

February 23, 2022

1  
2  
3 **Crumbs complex-directed apical membrane dynamics in epithelial cell**  
4 **ingression**

5  
6 Sérgio Simões<sup>1</sup>, Gerald Lerchbaumer<sup>1</sup>, Milena Pellikka<sup>1</sup>, Paraskevi Giannatou<sup>1</sup>, Thomas Lam<sup>1</sup>,  
7 Dohyun Kim<sup>1</sup>, Jessica Yu<sup>1,2,#</sup>, David ter Stal<sup>1</sup>, Kenana Al Kakouni<sup>1</sup>, Rodrigo Fernandez-  
8 Gonzalez<sup>1,2,3,4</sup>, Ulrich Tepass<sup>1,\*</sup>

9  
10 (1) Department of Cell and Systems Biology, University of Toronto; Toronto, ON M5S 3G5,  
11 Canada

12 (2) Institute of Biomedical Engineering, University of Toronto; Toronto, ON M5S 3G9, Canada

13 (3) Ted Rogers Centre for Heart Research, University of Toronto; Toronto, ON M5G 1M1,  
14 Canada

15 (4) Developmental and Stem Cell Biology Program, The Hospital for Sick Children; Toronto,  
16 ON M5G 1X8, Canada

17 (#) Present address: School of Biomedical Engineering at the University of British Columbia;  
18 Vancouver BC, V6T 1Z3, Canada

19 \* Corresponding author

20  
**Correspondence should be addressed to:**

Ulrich Tepass  
ORCID: 0000-0002-7494-5942  
Department of Cell and Systems Biology  
University of Toronto  
25 Harbord Street  
Toronto, Ontario M5S 2M6  
Canada

**Phone** (all authors except JY and RFG): 416-  
978-5712

**Phone** (JY and RFG): 416-978-7368

**Emails**

sergio.zallenlab@gmail.com  
gerald.lerchbaumer@mail.utoronto.ca  
milena.pellikka@utoronto.ca  
giannatou.evie@gmail.com  
lam.thomas1996@gmail.com  
kkdh1109@hotmail.com  
yu.jessica@ubc.ca  
david.terstal@utoronto.ca  
kenana.alkakouni@utoronto.ca  
rodrigo.fernandez.gonzalez@utoronto.ca  
u.tepass@utoronto.ca

**ORCID IDs**

SS: 0000-0002-0230-8813

UT: 0000-0002-7494-5942

## 22 **Abstract**

23 Epithelial cells often leave their tissue context and ingress to form new cell types or acquire  
24 migratory ability to move to distant sites during development and tumor progression. Cells lose  
25 their apical membrane and epithelial adherens junctions during ingression. However, how factors  
26 that organize apical-basal polarity contribute to ingression is unknown. Here, we show that the  
27 dynamic regulation of the apical Crumbs polarity complex is crucial for normal neural stem cell  
28 ingression. Crumbs endocytosis and recycling allow ingression to occur in a normal timeframe.  
29 During early ingression, Crumbs and its complex partner the RhoGEF Cysts support myosin and  
30 apical constriction to ensure robust ingression dynamics. During late ingression, the E3-ubiquitin  
31 ligase Neuralized facilitates the disassembly of the Crumbs complex and the rapid endocytic  
32 removal of the apical cell domain. Our findings reveal a mechanism integrating cell fate, apical  
33 polarity, endocytosis, vesicle trafficking, and actomyosin contractility to promote cell ingression,  
34 a fundamental morphogenetic process observed in animal development and cancer.

35

36

37 **Short title:** Crumbs complex function in cell ingression.

38

39 **Keywords:** Epithelial-mesenchymal transition, cell ingression, cell delamination, apical-basal  
40 polarity, Crumbs, neural stem cells, Live image analysis, *Drosophila*

41

## 42 **Main Text**

### 43 **Introduction**

44 The loss of apical-basal polarity and cell junctions are key early steps in epithelial to mesenchymal  
45 transitions (EMT) when cells leave the epithelium [Hay, 1995; Nieto et al., 2016; Campbell, 2018;  
46 Yang et al., 2020; Lambert and Weinberg, 2021]. EMTs drive cell escape during epithelial tumour  
47 progression and are frequent in animal development. Examples include the ingression of primary  
48 mesenchyme cells in the sea urchin embryo, the formation of mesoderm and endoderm during bird  
49 and mouse gastrulation, and the emergence of the neural crest in the vertebrate embryo [Shook  
50 and Keller, 2003; Lim and Thiery, 2012; Serrano-Najera and Weijer, 2020; Sheng, 2021]. In the  
51 *Drosophila* embryo, EMT is observed during mesoderm and endoderm development [Campbell et  
52 al., 2011; Gheisari et al., 2020] and in the neuroepithelium [Hartenstein and Wodarz, 2013]. We  
53 use the ingression of neural stem cells (or neuroblasts, NBs) as a model to study the mechanisms

54 regulating an EMT-like process [Simoes et al., 2017; An et al., 2017]. Our analysis revealed that  
55 the reduction of the apical surface of NBs is driven by 10-12 oscillating ratcheted contractions of  
56 actomyosin and the progressive loss of adherens junctions (AJs) to neighboring neuroepithelial  
57 cells.

58  
59 Epithelial polarity is governed by a network of polarity factors [Tepass, 2012; Rodriguez-Boulan  
60 and Macara, 2014; Pickett et al., 2019]. Here we investigate how the Crumbs (Crb) complex  
61 contributes to the loss of the apical domain – the apical membrane and AJs – during ingression.  
62 Crb is a transmembrane protein that governs apical membrane stability and the integrity of the  
63 circumferential AJs [Tepass et al., 1990; Wodarz et al., 1995; Tepass, 1996; Grawe et al., 1996;  
64 Silver et al., 2019]. Crb plays multiple roles in support of apical-basal polarity. It interacts with  
65 Moesin and the Spectrin cytoskeleton to support the apical cytocortex [Pellikka et al., 2002;  
66 Medina et al., 2002]. It interacts with the apical Par polarity complex including atypical Protein  
67 Kinase C (aPKC), which prevents apical enrichment of basolateral polarity proteins such as Lethal  
68 giant larvae or Yurt [Tepass, 2012; Morais-de-Sa et al., 2010, Pichaud et al., 2019; Gamblin et al.,  
69 2014]. Crb and its binding partners also recruit the RhoGEF Cysts (Cyst) to the apical junction.  
70 Cyst supports Rho1 activity and junctional myosin II, thus coupling Crb to junctional myosin  
71 stability [Silver et al., 2019]. Here, we have investigated how Crb contributes to the ordered  
72 reduction and ultimate removal of the apical domain during NB ingression.

## 73 74 **Results**

### 75 **Crumbs and E-cadherin are lost from the NB apical domain with different kinetics**

76 Neurogenesis in the *Drosophila* embryo is initiated by the emergence of NBs from the  
77 neuroectodermal epithelium (Fig. 1A) [Hartenstein and Wodarz, 2013]. Most NBs ingress from  
78 the epithelium as individual cells, a ~30 minute process during which NBs lose apical-basal  
79 polarity [Simoes et al., 2017; An et al., 2017]. NBs lose their apical membrane including Crb as  
80 they ingress [Tepass et al., 1990], and remove their apical E-cadherin (Ecad)-based AJ [Tepass et  
81 al., 1996]. (Fig. 1B). Interestingly, we noticed a marked difference in how these two  
82 transmembrane proteins are lost. The concentration of junctional Ecad remained relatively  
83 constant during ingression showing only an 1.12±0.28 fold change over time (Fig. 1B,C) [Simoes  
84 et al., 2017], whereas junctional Crb increased 1.35±0.65 fold (Fig. 1B,C). In addition, while

85 total apical Ecad levels declined in conjunction with apical area reduction, Crb total apical levels  
86 remained constant during the first 20 minutes (= ‘early ingression’) before declining rapidly during  
87 the last 10 minutes of apical area loss (= ‘late ingression’) (Fig. 1A-D). This suggests that Ecad  
88 and Crb are removed from the apical domain of NBs by distinct mechanisms.

89  
90 A series of ratcheted actomyosin contractions which become progressively stronger during  
91 ingression promote apical area loss of NBs [Simoes et al., 2017] (Figs. 1D,E; S1A). Notably,  
92 contraction-expansion cycles, which are ~2.5 minutes in length, correlate with fluctuations in Crb  
93 surface levels. 79.5% of apical contractions resulted in a reduction of Crb by 13.5±11% each,  
94 whereas Crb levels increased by a similar degree during 76.4% of apical expansions, resulting in  
95 the maintenance of apical Crb levels during early ingression. In contrast, during late ingression,  
96 89.6% of apical contractions reduced total apical Crb levels by 29±18% each, and a larger  
97 fraction of apical expansions (41.3% compared to 23.6% during early ingression) also contributed  
98 to Crb loss (Figs. 1E-G; S1A). Thus, Crb is actively removed from the membrane during  
99 contraction and secreted during expansion (Fig. 1G). The balanced decrease of Crb during  
100 contraction and increase during expansion in early ingression is consistent with normal protein  
101 turnover that maintains a uniform surface level. However, the shift to enhanced reduction of Crb  
102 during both contraction and expansion during late ingression suggests a change in the underlying  
103 mechanism of how Crb surface stability is regulated.

104

### 105 **Loss of Crb from the NB apical membrane promotes cell ingression**

106 Crb stabilizes the apical membrane of epithelial cells and is lost during ingression [Tepass et al.,  
107 1990; Wodarz et al., 1995]. We overexpressed Crb to test whether its loss is required for normal  
108 ingression. Crb overexpression consistently slowed ingression rates (Figs. 2A-C), causing a 57%  
109 increase in the amplitude of apical expansions and a 32% reduction in the duration of apical  
110 contractions (Fig. 2D), response parameters that varied with the level of overexpression. To ask  
111 how persistence of Crb interferes with ingression we examined Ecad and myosin II distribution.  
112 Increasing Crb reduced Ecad levels and disrupted the apical AJ with Ecad spreading through the  
113 lateral membrane (Figs. 2E). Crb overexpression also caused a decrease in junctional myosin and  
114 an increase in medial myosin levels (Fig. 2F). Moreover, NBs in Crb overexpressing embryos  
115 displayed unstable medial myosin networks, with higher rates of medial myosin assembly and

116 disassembly compared to controls (Fig. 2G,H). These results suggest that elevated levels of Crb  
117 delay ingression by favoring apical expansions through the apparent destabilization of junctional  
118 and medial myosin networks, which both contribute to the apical constrictions of ingressing NBs  
119 [Simoes et al., 2017].

120  
121 The persistence of apical Crb for much of the ingression process raises the question whether Crb  
122 plays an active role during NB ingression. Notably, NBs tended to ingress faster in Crb-depleted  
123 embryos (Figs 3A; S1B,C), although average ingression rates did not show a significant difference  
124 (Fig. 3B). However, we found a wider range in the rates of apical area loss in Crb-depleted embryos  
125 (0.2-6.2  $\mu\text{m}^2/\text{min}$ ) compared to controls (0.2-3.8  $\mu\text{m}^2/\text{min}$ ) (as assessed with an F-test; Fig. 3B).  
126 25% of NBs ingressed much faster on average upon loss of Crb than controls (2.6-6.2  $\mu\text{m}^2/\text{min}$   
127 versus 1.9-3.8  $\mu\text{m}^2/\text{min}$ , respectively) (Fig. 3B,C). NBs ingressing faster displayed a 3-fold  
128 increase in the amplitude of apical contractions, which also lasted 38% longer than in slower NBs  
129 (Fig. S1D). These findings indicate that Crb surface levels are an important determinant of  
130 ingression dynamics and ensure that NBs across the neuroepithelium complete ingression in a  
131 narrow time window.

132  
133 Loss of Crb resulted in a significant decrease in the amount of junctional myosin in ingressing  
134 cells, and also led to a moderate increase in medial myosin levels compared to controls (Figs. 3D;  
135 S1C). Both, fast and slow NBs showed enhanced rates of medial myosin assembly compared to  
136 controls, but in slow cells medial myosin was less stable due to higher disassembly rates (Fig.  
137 S1E,F). In addition, Crb-depleted NBs had reduced Ecad (Fig. 3E), with fast ingressing cells  
138 having significantly lower Ecad levels than slow cells (Fig. S1G). Thus, reduction in Ecad and  
139 junctional myosin levels, and greater variation in medial myosin disassembly rates may cause the  
140 enhanced variability in ingression dynamics in embryos lacking Crb.

141  
142 To test whether reduction of junctional myosin associated with loss of Crb is responsible for the  
143 differences in NB ingression dynamics we examined NBs in embryos depleted of the RhoGEF  
144 Cyst. Crb recruits Cyst to the apical junctions where Cyst stimulates the Rho1-Rho kinase-myosin  
145 II pathway (Fig. 2F) [Silver et al., 2019]. Loss of Cyst reduces junctional myosin in the  
146 neuroepithelium to a similar degree as observed in Crb-depleted embryos [Silver et al., 2019;

147 Garcia De Las Bayonas et al., 2019]. Thus, analysis of Cyst allowed us to isolate the impact Crb  
148 has on myosin from its other interactions with the Par6/aPKC complex, Moesin, or  $\beta$ <sub>H</sub>-Spectrin  
149 (Fig. 2F) [Tepass, 2012]. NB ingression speed in embryos lacking Cyst was consistently faster  
150 than controls, and did not show the variability observed upon the loss of Crb (Fig. 2B,G). Thus,  
151 isolating the impact of Crb on junctional myosin from other Crb activities through removal of Cyst  
152 revealed that the Crb-mediated stabilization of junctional myosin reduces ingression speed.

153

154 Ingression speed and the periodicity of apical contractions of NBs depend on the resistance and  
155 pulling forces exerted by neighboring non-ingressing cells (NICs) as NICs themselves undergo  
156 oscillating actomyosin contractions [Simoes et al., 2017]. Like NBs, NICs in Crb-depleted  
157 embryos display higher levels of medial myosin and lower levels of junctional myosin compared  
158 to controls [Silver et al., 2019], raising the possibility that defects in force balance between NBs  
159 and NICs could contribute to increased variation in ingression speed between NBs. We tested this  
160 hypothesis by comparing junctional and medial myosin pools between NBs and their surrounding  
161 NICs. In controls, the NB/NIC ratios of junctional or medial myosin levels positively correlated  
162 with ingression speed. In contrast, ingression speed in Crb-depleted embryos only positively  
163 correlated with medial but not junctional NB/NIC myosin ratios (Fig. S2).

164

165 Taken together, our findings support the view that a balance of NB intrinsic and extrinsic forces  
166 affect ingression speed. Because the reduction of junctional myosin seen in NBs and NICs upon  
167 loss of Crb or Cyst accelerates ingression in many NBs rather than slowing it down, we suggest  
168 that the reduced junctional myosin in NICs dominates the impact on ingression, reducing the  
169 resistance to apical constriction of NBs, thereby causing ingression in many NBs to speed up. The  
170 greater variability in ingression speed seen with the loss of Crb compared to the loss of Cyst may  
171 indicate that additional Crb functions contribute to the regulation of NB ingression. Thus, Crb  
172 persistence during early ingression with normal protein turnover rates ensures robust ingression  
173 dynamics and ingression in a normal timeframe.

174

### 175 **Crb ubiquitination-driven endocytosis is essential for NB ingression**

176 One striking observation during late ingression was the enrichment of prominent Crb-positive  
177 cytoplasmic puncta within NBs (Fig. 4A,C). These puncta were mature endosomes as

178 colocalization was observed with the endosomal markers Hrs, Vps26, Rab5, and Rab7 among  
179 others (Figs. 4B,D; S3), suggesting that Crb is removed from the plasma membrane through  
180 endocytosis. These endosomes were also enriched in Ecad and the Notch ligand Delta, which  
181 signals to surrounding NICs resulting in an epidermal fate [Hartenstein and Wodarz, 2013] (Fig.  
182 4B,D). Crb-positive endosomes persisted in NBs for some time after ingression was completed  
183 (Figs. 4A; S3Q,R).

184

185 How does Crb endocytosis impact NB ingression? To address this question we generated a form  
186 of Crb that showed strongly reduced endocytosis. The 37 amino acid cytoplasmic tail of Crb  
187 contains two Lysine (K) residues. K residues are potential targets for ubiquitination, which signals  
188 endocytosis [Haglund and Dikic, 2012]. K by Arginine (R) exchange to block potential  
189 ubiquitination of Crb (GFP::CrbRR) resulted in an excessive apical accumulation of GFP::CrbRR  
190 during both early and late ingression (Fig. 4E,G), and its persistence in the NB plasma membrane  
191 well after ingression (95/115 S1 NBs at stage 9), rather than a translocation into endosomes as  
192 seen with GFP::Crb (84/84 NBs; Fig. 4F). GFP::CrbRR also accumulated at the cortex of NICs,  
193 which caused an excessive apicalization as was reported for Crb overexpression [Wodarz et al.,  
194 1995]. These results suggest that ubiquitination of Crb is an important signal for its internalization.

195

196 GFP::CrbRR expression caused a failure of ingression in ~25% of NBs, marked by a NB-type  
197 division within the neuroepithelium, which normally occurs after ingression below the epithelium  
198 (Fig. 4E-bottom panels; Sup. Videos 1 and 2). ~75% of NBs ingressed successfully but took twice  
199 as long to complete ingression (Fig. 4E-middle panels, H; Sup. Videos 1 and 3). Blocking Crb  
200 endocytosis also reduced the duration and amplitude of apical contractions in ingressing NBs by  
201 19% and 15%, respectively, relative to control NBs expressing GFP::Crb (Fig. 4I,J). These results  
202 indicate that Crb ubiquitination and subsequent endocytosis are crucial for apical membrane  
203 dynamics during early and late NB ingression, and that Crb ubiquitination is a key molecular  
204 determinant of normal ingression.

205

### 206 **Endocytosis, degradation, and recycling regulate NB ingression**

207 To better understand how endocytosis contributes to the removal of the apical domain during NB  
208 ingression, we tracked membrane internalization using the lyophilic dye FM4-64 [Rigal et al.,

209 [2015] and quantified its incorporation into newly formed endosomes (Fig. 5A,B). Irrespective of  
210 injecting FM4-64 into the perivitelline space or inside the embryo (facing the apical or basal side  
211 of the neuroepithelium, respectively) newly formed endosomes originated within 1.0-6.5  $\mu\text{m}$   
212 below the apical plasma membrane (total cell depth:  $\sim 30 \mu\text{m}$ ), indicating that endocytosis  
213 predominantly occurs apically (Sup. Video 4). Interestingly, we found that the density of apical  
214 FM4-64 positive vesicles increased in NBs during late ingression but remained constant in NICs  
215 (Fig. 5A,B; Sup. Video 5). These findings are consistent with an enhanced accumulation of  
216 GFP::Dynamamin and GFP::Clathrin, two endocytotic markers [Mettlen et al., 2018], at the NB apical  
217 domain compared with NICs (Fig. 5C-F). We conclude that the enhanced apical contractions  
218 observed during NB ingression [Simoes et al., 2017; An et al., 2017] correlate with an increase in  
219 apical endocytosis.

220

221 We next reduced endocytosis by knockdown of the endocytic adaptor AP2 $\alpha$ , which interacts with  
222 Crb [Lin et al., 2015], or by using a thermosensitive Dynamamin allele (Dyn<sup>TS</sup>). AP2 $\alpha$  depletion  
223 reduced the amplitude of apical contractions in NBs by 34% whereas amplitude of expansion and  
224 the duration of contractions and expansions remained normal (Fig. 6A,B). This reduced ingression  
225 speed (Fig. 6A- bottom panels), or prevented ingression of 38% of NBs, which divided on the  
226 embryo surface (Fig. 6A-middle panels; Sup. Videos 6-8). Dyn<sup>TS</sup> embryos grown at the restrictive  
227 temperature from the onset of ingression showed a delay in apical domain loss (Figs. 6C; S4). 56%  
228 of NBs constricted apically but failed to complete ingression and 22% of NBs divided within the  
229 neuroepithelium. Blocking Dynamamin also resulted in elevated apical Crb and Ecad concentrations  
230 in ingressing NBs (Figs. 6C; S4). Conversely, we increased apical endocytosis through the  
231 expression of a constitutively active form of the early endocytic regulator Rab5 (Rab5-CA). This  
232 accelerated the rate of apical membrane removal 1.8-fold, increased the amplitude of apical  
233 contractions by 38% and decreased the duration of apical expansions by 21%, relative to controls  
234 (Fig. 6D). Together, these results highlight a pivotal role for early endocytic regulators in directing  
235 Crb internalization and in regulating the ratcheted contractions that drive NB apical domain loss.

236

237 Endosomal Crb colocalizes with Hrs, a component of the ESCRT complex which facilitates late  
238 endosomal/lysosomal processing and protein degradation [Vietri et al., 2020], and Vps26, a  
239 component of the Retromer complex that is crucial for maintaining Crb surface levels in the



240 neuroepithelium through recycling [Zhou et al 2011; Pocha et al., 2011; McNally and Cullen,  
241 2018]. We therefore assessed whether ESCRT or Retromer function is required for NB ingression.  
242 Strikingly, loss of Retromer function, which reduced Crb levels by half both apically and  
243 intracellularly in NBs, strongly accelerated ingression by 67% ( $2.5 \pm 0.9 \mu\text{m}^2/\text{min}$  versus  $1.5 \pm$   
244  $0.9 \mu\text{m}^2/\text{min}$  in controls) (Fig. 6E). This shows that recycling is crucial for maintaining Crb surface  
245 levels in NBs similar to the neuroepithelium as a whole, and indicates that Retromer-mediated  
246 recycling counteracts the loss of the apical domain. The faster ingression seen with the loss of  
247 Retromer function compared to the loss of Crb (Fig. 6E versus Fig. 3A) suggests that the Retromer  
248 complex recycles additional factors that stabilize the apical domain of NBs. Ecad, which  
249 colocalizes with Crb in NB endosomes (Fig. 4B,D) is an attractive candidate. In contrast to  
250 Retromer, blocking the ESCRT complex by removing Hrs function had no major impact on  
251 ingression dynamics. NBs tended to ingress slower in these embryos, a delay that may be specific  
252 to late ingression (Fig. 6F), when Crb and other transmembrane proteins are normally rapidly  
253 translocated from the apical domain into an ESCRT-positive endocytic compartment. NBs in  
254 embryos that lack ESCRT function retained apical Crb 15 minutes longer than control NBs and  
255 displayed reduced intracellular Crb accumulation in a more diffuse pattern than controls (Fig. 6F).  
256 We conclude that ESCRT and Retromer machineries are important determinants of NB ingression  
257 dynamics.

258

### 259 **Neutralized resolves the Crb-Sdt complex for rapid internalization of Crb during late** 260 **ingression**

261 Our analysis suggests that the rapid loss of Crb from the NB apical membrane during late  
262 ingression is crucial for delamination. This raises the question of how Crb can deviate from steady-  
263 state turn-over to be completely removed from the membrane. In embryos lacking the Crb-binding  
264 partner Sdt, Crb is unstable and rapidly endocytosed [Tepass and Knust, 1993]. We confirmed  
265 these results with live-imaging of Crb::GFP in embryos lacking Sdt. Loss of Sdt rendered Crb  
266 mostly endocytotic across the neuroepithelium. In contrast, non-endocytosable GFP::CrbRR  
267 remained at the plasma membrane in Sdt-depleted embryos (Fig. S5A). Loss of Sdt increased late  
268 ingression speed by two-fold, while having no net effect on early ingression (Fig. 7A). We  
269 conclude that destabilization of the Crb-Sdt interaction promotes Crb endocytosis and apical  
270 domain loss specifically during late ingression.

271  
272 Endocytosis of Crb is fostered by the E3 Ubiquitin ligase Neuralized (Neur) via interaction with  
273 an isoform of Sdt containing sequences encoded by its exon 3 (Sdt3) [Perez-Mockus et al., 2017a].  
274 Interestingly, overactivation of Neur disrupts epithelial polarity through a deactivation of Sdt,  
275 precipitating the loss of Crb [Chanet and Schweisguth, 2012; Perez-Mockus et al., 2017a]. Sdt3 is  
276 one of multiple Sdt alternative splice forms [Bulgakova et al., 2010; Perez-Mockus et al., 2017a].  
277 Quantitative imaging of total endogenous Sdt (Sdt::GFP) and Sdt3::GFP, a construct where only  
278 the endogenous Sdt3 isoform is GFP-tagged, revealed that Sdt3 represented ~79% of the total  
279 apical Sdt during early ingression but was the only Sdt isoform present in NBs during late  
280 ingression (Fig. 7B). Thus, we explored the possibility that the Sdt3-Neur interaction could  
281 mediate Crb endocytosis and apical domain loss during late NB ingression.

282  
283 NBs from embryos expressing Sdt3::GFP completely lost their apical domain within ~30 minutes  
284 as in normal embryos (Fig. 7C; Sup. Video 9). Also NBs in embryos expressing an isoform of Sdt  
285 lacking exon 3 (Sdt $\Delta$ 3::GFP), which abrogates the interaction between Sdt3 and Neur [Perez-  
286 Mockus et al., 2017a], constricted their apical domain in a normal timeframe (Fig. 7D). However,  
287 Sdt $\Delta$ 3::GFP NBs failed to fully internalize the apical membrane and retained small ‘apical plugs’  
288 that persisted for an extended period of time. These apical plugs were spherical, with a total surface  
289 of  $6.2 \pm 3 \mu\text{m}^2$  representing ~15% of the initial apical cell surface and remained detectable for at  
290 least 40 minutes beyond normal ingression time (Fig. 7C,E; Sup. Video 10). Sdt $\Delta$ 3::GFP showed  
291 similar apical protein levels to Sdt3::GFP at early ingression but was less efficiently removed from  
292 the apical cortex during late ingression (Fig. 7F), and apical plugs in Sdt $\Delta$ 3::GFP embryos  
293 accumulated high levels of Sdt $\Delta$ 3::GFP and Crb (Fig. 7H). Ecad was confined to a narrow neck  
294 below the plug (Fig. 7I) as the main cell body of the NB moved below the epithelium, and AJs  
295 disassembled shortly thereafter. Apical plugs remained at the embryo surface suggesting that they  
296 detached from the main cell body of the NBs. Plugs were ultimately resolved. The abnormal  
297 accumulation of apical Crb and Sdt $\Delta$ 3::GFP correlated with a deceleration in apical area loss  
298 during late ingression relative to Sdt3::GFP controls (Fig. 7G). These findings indicate a specific  
299 defect in internalization of Crb and apical membrane loss when the Sdt3-Neur interaction is

300 blocked, and show that the Sdt3-Neur interaction is crucial for the removal of the NB apical  
301 domain during late ingression.

302

303 Neur is part of the Notch signalling pathway, promoting endocytosis of the Notch ligand Delta and,  
304 consequently, Notch activation and suppression of NB fate in NICs that surround a NB [Perez-  
305 Mockus and Schweisguth, 2017; Kovall et al., 2017]. Loss of Delta, Notch or Neur causes the  
306 formation of supernumerary NBs that ingress as clusters rather than as individual cells [Hartenstein  
307 and Wodarz, 2013; Simoes et al., 2017]. To validate that internalization of Crb was in part  
308 mediated by Neur, we examined Neur-depleted embryos in comparison to Delta-depleted embryos.  
309 Upon reaching an average apical surface of  $\sim 15 \mu\text{m}^2$  (late ingression), Neur-depleted NBs  
310 displayed more apical Crb, and ingression speed significantly decreased compared to NBs in  
311 Delta-depleted embryos indicating that Neur acts independent of Delta in disrupting the Crb  
312 complex (Figs. 8A-C, S5B). Loss of Neur led to a strong reduction in oscillations of apical  
313 contractions in NBs likely causing the delay in ingression (Fig. 8D). To directly test whether Neur  
314 promotes Crb endocytosis in ingressing NBs, we quantified total levels of endocytotic Crb in  
315 ingressed NBs from Neur-depleted embryos and Sdt3::GFP embryos. Both mutant backgrounds  
316 showed a significant reduction (14-26%) in total levels of internalized Crb compared to controls  
317 (Fig. 8E,F). Taken together, our findings suggest a novel function for the Sdt3-Neur interaction in  
318 driving the efficient removal of apical membrane during late NB ingression by promoting the  
319 disassembly of the Crb complex and, consequently, Crb endocytosis.

320

## 321 Discussion

322 Drosophila NBs are an outstanding model for scrutinizing the cellular machineries underpinning  
323 an EMT-like process with high temporal and spatial resolution. While ingressing, a single NB  
324 sequentially loses AJs responding to tensile forces exerted by two pools of actomyosin: a planar  
325 polarized pool enriched at anterior-posterior junctions, which disassembles first, and a pulsatile  
326 pool at the free apical cortex which further tugs on shrinking junctions in a ratchet-like manner  
327 [Simoes et al., 2017; An et al., 2017]. However, while actomyosin forces reduce the apical  
328 perimeter, it remained unclear how cells lost their apical domain and how polarity regulators  
329 contribute to the dynamics of apical domain loss. We demonstrate that regulation of the Crb  
330 complex plays a key role in orchestrating apical domain loss during ingression. During early

331 ingression, cells shrink their apical domain while retaining total levels of Crb, which is crucial for  
332 maintaining normal actomyosin in NBs and NICs to generate the tension balance required for  
333 normal ingression dynamics. During late ingression, Crb is rapidly lost from the apical domain, a  
334 process initiated by an interaction between Neur and Sdt which causes the disassembly of the Crb  
335 complex. The loss of the Crb complex then precipitates the concurrent loss of the apical membrane  
336 and AJs. A similar regulatory interplay between Crb, Sdt, and Neur was also observed during early  
337 neurogenesis in the *Drosophila* optic lobes [Shard et al., 2020]. Here, neural stem cells emerge  
338 from a wave front in the optic lobes rather than ingress as individual cells. Despite these  
339 topological differences, the Crb/Sdt/Neur module appears to be a common cell biological regulator  
340 of EMT during early neurogenesis.

341  
342 Endocytosis and endocytic degradation and recycling are requirements for normal NB ingression  
343 dynamics. The apical membrane of neuroepithelial cells is much more active endocytically than  
344 the basolateral membrane. Notably, Crb is endocytosed during apical contractions and re-secreted  
345 during expansions, suggesting that myosin-driven cell contact contraction promotes endocytosis,  
346 consistent with recent data from mammalian cells [Cavanaugh et al., 2020], whereas expansions  
347 allow for enhanced secretion. Blocking endocytosis increases surface levels of Crb and Ecad as  
348 expected, and prevents NB ingression, whereas enhancing endocytosis accelerates ingression.  
349 Moreover, endocytic trafficking plays a key role in determining ingression speed. Loss of ESCRT  
350 complex-mediated degradation appears to enhance apical Crb and slow ingression, whereas loss  
351 of Retromer-mediated recycling dramatically reduced surface Crb and accelerated ingression. In  
352 fact, Retromer-compromised embryos showed the fastest ingression speed of any condition we  
353 have examined, suggesting that the Retromer not only recycles Crb but also other factors that  
354 counteract apical domain loss in NBs. Crb turnover during early ingression maintains a steady Crb  
355 surface abundance. During late ingression, Crb endocytosis is enhanced during both apical  
356 contraction and expansion as a result of the disruption of the Crb-Sdt interaction by Neur, which  
357 likely makes the Crb cytoplasmic tail accessible to the Clathrin adapter AP2. AP2 binds to Crb  
358 competitively with Sdt [Lin et al., 2015], facilitating the rapid endocytic removal of Crb and the  
359 apical membrane.

360

361 EMT is thought to be initiated by the expression of EMT transcription factors (EMT-TFs) of the  
362 Snail, Zeb, or bHLH families that downregulate key adhesion or polarity proteins such as Ecad  
363 and Crb [Lamouille et al., 2014; Nieto et al., 2016; Dongre and Weinberg, 2019; Yang et al., 2020].  
364 NBs are specified through the combined action of proneural genes that include bHLH proteins of  
365 the Achaete-Scute complex (AS-C), the Snail family protein Wornui, and the SoxB family protein  
366 SoxNeuro [Hartenstein and Wodarz, 2013; Arefin et al., 2019]. However, although genes that  
367 encode Ecad and Crb are transcriptionally downregulated in NBs [Tepass et al., 1990; Tepass et  
368 al., 1996] this repression does not appear relevant for NB ingression. Replacing endogenous Ecad  
369 with a transgene expressing Ecad under the control of a ubiquitous promoter had no impact on NB  
370 ingression dynamics [Simoes et al., 2017]. Here, we show that surface levels of Crb remained high  
371 in NBs during early ingression before Crb is rapidly removed by endocytosis during late  
372 ingression. This raises the question of how the upregulation of proneural genes in presumptive  
373 NBs elicits enhanced actomyosin contractility and endocytic removal of apical membrane and  
374 junctions.

375

376 One proneural gene target is *neur* [Miller and Posakony, 2018; Arefin et al., 2019]. Neur is found  
377 throughout the neuroepithelium participating in Delta-Notch-mediated lateral inhibition to select  
378 the NB from an equivalence group of 5-7 cells [Boulianne et al., 1991; Hartenstein and Wodarz,  
379 2013]. *neur* upregulation in ingressing NBs is thought to be part of a positive feedback that  
380 stabilizes NB fate through persistent asymmetric Delta-Notch signalling [Miller and Posakony,  
381 2018; Arefin et al., 2019]. The increase in Neur may also be important for the effective disruption  
382 of the Crb complex to destabilize the apical domain. Neur can disrupt the Crb complex across the  
383 epithelium, but is normally prevented from doing so by Bearded proteins that act as inhibitors of  
384 Neur [Chanet and Schweisguth, 2012; Perez-Mockus et al., 2017a]. Increasing Neur concentration  
385 may overcome this inhibition in NBs. This raises the possibility that the proneural gene-dependent  
386 upregulation of *neur* contributes to the timing of ingression, consistent with our observation that  
387 in Neur-depleted embryos ingression is prolonged. Furthermore, Neur may enhance actomyosin  
388 contractility in NBs seen in late ingression [Simoes et al., 2017; An et al., 2017] as was reported  
389 for Neur in the *Drosophila* mesoderm [Perez-Mockus et al., 2017b]. We hypothesize therefore that  
390 Neur could be a central regulator of NB selection and ingression; stabilizing NB fate, driving apical  
391 membrane constriction through actomyosin contraction, and disrupting the Crb complex to remove

392 apical membrane and junctions. Interestingly, we also noted that during ingression the number of  
393 alternative isoforms of Sdt is limited to Sdt3, the isoform susceptible to Neur. Hence, NBs appear  
394 to develop the molecular competence for apical membrane removal at least in part through  
395 rebalancing Sdt splice forms.

396

397 The loss of apical-basal polarity is an early event during EMT marked by the loss of epithelial AJs  
398 that can trigger expression of EMT-TFs and the disassembly of cell junctions [Ozdamar et al.,  
399 2005; Jung et al., 2019]. However, our findings indicate that the loss of apical-basal polarity in  
400 NBs is preceded by a period (~20 min; early ingression) of ratcheted apical contractions that reduce  
401 the apical area of delaminating cells [Simoes et al., 2017; An et al., 2017]. The maintenance of  
402 normal Crb levels during early ingression is crucial for normal ingression dynamics. Crb stabilizes  
403 junctional myosin through its effector, Cyst that is recruited to the junctional domain by the Crb  
404 complex [Silver et al., 2019]. Whereas the loss of Crb or loss of Cyst causes similar reductions of  
405 junctional myosin in the neuroepithelium [Silver et al., 2019], NB ingression was consistently  
406 faster in Cyst-compromised embryos than controls. In contrast, NBs in Crb compromised embryos  
407 showed much larger variability of ingression speeds, with a small fraction of NBs ingressing  
408 rapidly while the majority was slower than controls. Thus, it is likely that Crb makes other  
409 contributions to regulating NB ingression in addition to its Cysts-mediated function in supporting  
410 junctional actomyosin. Interestingly, the mouse Crb homolog Crb2 is required for myosin  
411 organization and ingression during gastrulation [Ramkumar et al., 2016]. The predominant defect  
412 in Crb2 compromised mice appears to be a failure of ingression which may be similar to the  
413 fraction of NBs showing slower than normal ingression seen with the loss of *Drosophila* Crb. To  
414 what extent the differences in cell behaviour caused by the loss of Crb and Crb2 depend on the  
415 biomechanical specifics of the tissue context or result from differences in molecular pathways in  
416 which Crb and Crb2 operate remains to be explored.

417

418

## 419 **Materials and Methods**

420

### 421 **Markers and mutants**

422 The following fly markers and mutants were used: *w*<sup>1118</sup> as ‘wild type’ (Bloomington Drosophila  
423 Stock Center: BDSC\_3605), *endo-crumbs::GFP-C* [Huang et al., 2009], *endo-DEcad::GFP*  
424 (BDSC\_60584; gift from Y. Hong, University of Pittsburgh), *y w;ubi-DEcad::GFP* [Oda et al.,  
425 2001], *sqh-sqh::mCherry* [Martin et al., 2009] and *sqh-GAP43::mCherry* (gifts from A.C. Martin,  
426 Massachusetts Institute of Technology) [Martin et al., 2010], *w FRT18E Par6<sup>226</sup>*  
427 *P[promPar6\_Par6::GFP]61-1F* [Petronczki and Knoblich, 2001], *endo-Delta::GFP* [Corson et  
428 al., 2017], *sdt::GFP*, *sdt::GFP3*, and *sdtΔ3::GFP* (gifts from F. Schweisguth, Institut Pasteur,  
429 Paris) [Perez-Mockus et al., 2017a], *HG4-1* (gift from Chris Q. Doe, University of Oregon)  
430 [Hirono et al., 2012], *y w;; Mi(PT-GFSTF.1)kst<sup>MI03134-GFSTF.1</sup>* (BDSC\_60193), *y w shi<sup>ts1</sup>* (= *Dyn<sup>TS</sup>*;  
431 BDSC\_7068), *y w Vps26<sup>3c</sup> FRT101/FM7c* (a *Vps26* null allele; K.A.K and U.T., unpublished),  
432 *Hrs<sup>D28</sup>FRT40A/In(2LR)Gla*, *wg<sup>Gla-1</sup> PPO1<sup>Bc</sup>* (BDSC\_54574), *w;; crb<sup>11a22</sup> FRT82B/TM3 Sb*  
433 [Pellikka et al., 2002], *matatub67-Gal4*; *matatub15-Gal4* (gift of D. St Johnston, University of  
434 Cambridge, England, UK), *UAS-AP2α-RNAi* (BDSC\_32866, Trip line #HMS00653, Drosophila  
435 RNAi Screening Center, Harvard Medical School), *UASp-YFP::Rab5* (BDSC\_9775), *UASp-*  
436 *YFP::Rab5Q88L* (BDSC\_9773), *w; UAS-crb<sup>WT2e</sup>* [Wodarz et al., 1995], *w;; UAS-GFP::crb*  
437 (*attp2*) and *w;; UAS-GFP::crbRR (attp2)*, *UAS-Dcr-2*, *w<sup>1118</sup>* (BDSC\_24646), *w; UAS-GFP-myc-*  
438 *2XFYVE* (BL\_42712), *w; UAS-Rab7::GFP* (BDSC\_42705), *w; UAS-GFP::Lamp* (BDSC\_42714,  
439 gift from J. Brill, University of Toronto, Canada), *w; UAS-Rab11::GFP* (BDSC\_8506), *UAS-*  
440 *PLC&PH::eGFP* (BDSC\_39693), *UAS-IVS-Syn21-shi<sup>ts1</sup>::GFP-p10* [Pfeiffer et al., 2012], *UAS-*  
441 *eGFP::Clc* (BDSC\_7107) (gift from T. Lecuit, Institut de Biologie du Développement de  
442 Marseille).

443

444 To overexpress Crb maternally, we analyzed the progeny of *matatub67-Gal4 endo-*  
445 *DEcad::GFP/UAS-crb<sup>WT2e</sup>; sqh-sqh::mCherry/+* females crossed to *UAS-crb<sup>WT2e</sup>* homozygous  
446 males. Control embryos were the progeny of *matatub67-Gal4 endo-DEcad::GFP/+; sqh-*  
447 *Sqh::mCherry/+* females crossed to *w<sup>1118</sup>* males. Similarly, overexpression of *GFP::CrbRR* and  
448 *GFP::Crb* was obtained by crossing *matatub67-Gal4/+; matatub15-Gal4/UAS-GFP::crbRR* (or  
449 *GFP::crb*) females to *UAS-GFP::crbRR* (or *GFP::crb*) males. A similar genetic scheme was

450 employed to maternally express *UAS-GFP-myc-2XFYVE*, *UAS-Rab7::GFP*, *UAS-GFP::Lamp1*,  
451 *UAS-Rab11::GFP* and *UAS-PLC $\delta$ -PH::eGFP*. *Matatub15-Gal4* alone was used to drive the  
452 expression of *UASp-YFP::Rab5* (Fig. S3). *Matatub67-Gal4* recombined with *sqh-*  
453 *GAP43::mCherry* was used to drive the expression of *UAS-eGFP::Clc* (Fig. 5). *Matatub15-Gal4*  
454 recombined with *sqh-GAP43::mCherry* was used to drive the expression of *UASp-YFP::Rab5*,  
455 *UASp-YFP::Rab5Q88L* and *UAS-IVS-Syn21-shi<sup>ts1</sup>::GFP-p10* (Fig. 6 and Fig. S4).

456

457 To knockdown *cysts* in the maternal germline, we crossed *Matatub67-Gal4*, *endo-DEcad::GFP*  
458 (BDSC\_60584) with *Df(2L)BSC301* (a deletion uncovering *cysts*; BDSC\_23684); *UAS-cysts-*  
459 *shRNA* (BDSC\_41578). Female progeny of this cross were mated with *UAS-cysts-shRNA*  
460 (BDSC\_38292) males and ingression dynamics of NBs were analyzed in the resulting progeny.

461

462 To down-regulate Dynamin function and visualize NBs in fixed embryos, 0-3 hours after egg  
463 laying (AEL) *Dyn<sup>TS</sup>* (= *shi<sup>ts1</sup>*); *HG4-1* embryos (laid at 18°C) were aged for 1.5 hours at 22°C and  
464 either kept at 22°C (permissive temperature) or transferred to 32°C (restrictive temperature) for 3  
465 hours before fixation.

466

467 To knockdown *AP2 $\alpha$*  during ingression, we analyzed the F2 progeny of *matatub15-Gal4 sqh-*  
468 *GAP43::mCherry* females crossed to *UAS-AP2 $\alpha$ -RNAi* males. Control embryos were generated  
469 similarly by using *w<sup>1118</sup>* males. Females carrying *Vps26<sup>3c</sup>* and *Hrs<sup>D28</sup>* germline clones expressing  
470 *endo-crb::GFP* were generated using the FLP-DFS system [Chou and Perrimon, 1996]. Their  
471 respective wild-type controls expressing *endo-crb::GFP* were imaged in parallel using the same  
472 conditions.

473

## 474 Immunohistochemistry

475 Embryos were fixed in a 1:1 mixture of 3.7% formaldehyde in phosphate buffer, pH 7.4, and  
476 heptane for 20 minutes under agitation, and devitellinized with a methanol/heptane mixture  
477 (Method A) or a 1:1 mixture of 37% formaldehyde and n-heptane for 5 minutes, followed by hand-  
478 devitellization (Method B). Method A was used in Fig. 4A, Fig. 4B (to detect Delta::GFP); Fig.  
479 4F; Fig. 6C, E, and F; Fig. 7H, I; Fig 8E; Fig. 2E; Fig. S3A-D, F-J, L, and M. Method B was used  
480 in Fig. 4B (to detect Hrs, Vps26 and Ecad::GFP); Fig. 8F; Fig S1B; Fig. S3E, K, and N; Fig. S5B.



481  
482 The following antibodies were used: rabbit anti-GFP, 1:150 (Torrey Pines), guinea pig anti-Snail,  
483 1:100 (a gift from E. Wieschaus), rat anti-DEcad2, 1:25 (Developmental Studies Hybridoma Bank,  
484 DSHB), mouse anti-Dlg, 1:50 (DSHB), rat anti-Crumbs 1:100 [Pellikka et al., 2002], mouse anti-  
485 Arm, 1:25 (DSHB), guinea pig anti-Hrs, 1:500 and guinea pig anti-Vps26, 1:500 (gifts from H.  
486 Bellen, Baylor College of Medicine, HHMI) [Wang et al., 2014], rabbit anti-beta-Galactosidase,  
487 1:100 (Cappel), rabbit anti-Sdt, 1:3000 (gift from E. Knust, MPI CBG) [Bachmann et al., 2001],  
488 rabbit anti-PKC $\zeta$ , 1:500 (C-20, Santa Cruz), guinea pig anti-Baz, 1:500 (gift from J. Zallen,  
489 MSKCC, HHMI) and rabbit anti-P-Ezrin/ERM (T567), 1:100 (Cell Signalling, 48G2). Secondary  
490 antibodies conjugated to Alexa Fluor 488, Alexa Fluor 568, or Alexa Fluor 647 (Molecular Probes)  
491 were used at 1:400.

492  
493 Embryos were mounted in Prolong Gold (Molecular Probes) and imaged with zoom factors  
494 ranging from 0.75 to 3 on a TCS SP8 Leica resonant scanning confocal microscope with a HCX  
495 PL APO 63X/1.4NA CS2 objective (Leica Microsystems) via sequential scanning between  
496 channels. 1  $\mu$ m Z-slices were acquired at 0.37  $\mu$ m steps. Maximum projections of 2-3  $\mu$ m including  
497 the apical domain or the cell nuclei were analyzed. As the rat anti-Crb antibody can detect  
498 intracellular Wolbachia (which resemble endocytic vesicles) in infected *Drosophila* stocks, we  
499 treated adult flies with Tetracycline at 1.5 mg/ml in food or yeast paste for 4-5 days prior to egg  
500 collection, in order to eliminate this symbiont. To select *crb*<sup>11a22</sup> homozygous embryos expressing  
501 GFP::Crb or GFP::CrbRR (Fig. 4F), we employed LacZ staining in the progeny from *matatub67-*  
502 *Gal4/+; crb*<sup>11a22</sup> *FRT82B UAS-GFP::Crb* (or *UAS-GFP::CrbRR*)/*TM3, Sb hb-LacZ* females  
503 crossed to *crb*<sup>11a22</sup> *FRT82B/ TM3, Sb hb-LacZ* males. Cross-section views of the ectoderm in Fig.  
504 2E were obtained by cutting stained embryos manually with a 27-gauge syringe.

505

### 506 Time-lapse imaging

507 Embryos expressing the indicated fluorescent markers were dechorionated for 2 minutes in 50%  
508 bleach, transferred to a drop of halocarbon oil 27 (Sigma) on a coverslip, and mounted on an  
509 oxygen-permeable membrane (YSI). GFP was excited with an OPSL 488 nm laser (2-3.5%) and  
510 mCherry was excited with an OPSL 514 nm laser (3-5%). A HCX PL APO 63X/1.4NA CS2  
511 objective on a TCS SP8 Leica resonant scanning confocal microscope (Leica Microsystems) was

512 used for imaging. 12-bit images of one or 2-color Z-stacks (5-13 planes; optical sections: 1.1-1.3  
513  $\mu\text{m}$ ) were acquired at 0.45-0.5  $\mu\text{m}$  steps every 4, 6, 10 or 15 sec intervals and maximally projected  
514 for analysis. Pixel dimensions ranged from 144 to 360 nm/pixel.

515

516 To image the consequences of the loss of Dynamin function ( $\text{Dyn}^{\text{TS}}$ ), *shi<sup>ts1</sup>* embryos expressing  
517 *ubi-DEcad::GFP* or *endo-crb::GFP* were aged until mid-stage 7 (3h15 AEL) or mid-stage 8 (3h30  
518 AEL) and imaged at 22°C (permissive temperature) or 32°C (restrictive temperature) using a stage  
519 top incubator (TOKAI HIT) assembled onto the TCS SP8 Leica resonant scanning confocal  
520 microscope.

521

### 522 **dsRNA and FM4-64 injections**

523 Templates to produce dsRNA against *crb*, *sdt*, *neur* and *Dl* were generated by PCR from genomic  
524 DNA, using the following pairs of primers containing the T7 promoter sequence (5'-  
525 TAATACGACTCACTATAGGGAGACCAC-3') at the 5' end:

526 Crb fw: 5'CGAGCCATGTCGGAATGGATCAACC 3'

527 Crb rv: 5'GTCGCTCTTCCGGCGGTGGCTTCAG 3'

528 Sdt fw: 5' CCGTGGTACCACCGCCACTGGCGC 3'

529 Sdt rv: 5' CACCCAACCCGGCCAGTTGACTGC 3'

530 Neur fw: 5' CGTACGGAATCTGACTTCTGCCAGGG 3'

531 Neur rv: 5' CTCGATGTACTGGCTGCTGGTGGTGC 3'

532 Delta fw: 5'GGAGCCTTGTGCAACGAGTGCGTTC3'

533 Delta rv: 5'CGCACGACAGGTGCACTGGTAATCG3'

534

535 PCR products were used as templates for T7 transcription reactions with the 5 $\times$  MEGAscript T7  
536 kit (Ambion). dsRNA was injected dorsally in 0-1 hour old embryos from the stocks *w; endo-*  
537 *DEcad::GFP; sqh-sqh:mCherry* (for *crb*-RNAi and *sdt*-RNAi) and progeny of *UAS-Dicer2/+;*  
538 *matatub67-Gal4/+; matatub15-Gal4/endo-crb::GFP* females crossed to *endo-crb::GFP* males  
539 (for *neur*- and *Dl*-RNAi).

540

541 Embryos were dechorionated, glued to a coverslip, dehydrated for 5 minutes, covered in 1:1  
542 halocarbon oil 27/700 (Sigma), and injected with 100–200 pl of 1–2.0  $\mu\text{g}/\mu\text{l}$  of dsRNA each.

543 Control embryos were injected with water or not injected, as indicated. Embryos were incubated  
544 in a humidified chamber at 25°C and imaged between stages 7-9. For immunostaining, embryos  
545 were washed off the coverslip with n-heptane at stages 8 to 9, fixed for 5 minutes in 37%  
546 formaldehyde in PBS/heptane and manually devitellinized.

547

548 To visualize apical membrane internalization during ingression (**Fig. 5A,B**), we injected *w<sup>1118</sup>*  
549 embryos dorsally with 100–200 pL of FM4-64 at 8 mM dissolved in 50% DMSO, either into the  
550 perivitelline space, or directly inside the embryo, and immediately imaged live using the 514 nm  
551 laser.

552

### 553 **Cell Segmentation and fluorescence quantification**

554 We used SIESTA to automatically identify cell outlines in time-lapse movies using a watershed  
555 algorithm as described [[Fernandez-Gonzalez and Zallen, 2015](#); [Leung and Fernandez-Gonzalez,](#)  
556 [2015](#)]. When manual correction was necessary, a semi-automated method of manual tracing of cell  
557 interfaces included in SIESTA, the LiveWire, was used [[Fernandez-Gonzalez and Zallen, 2013](#)].

558

559 To measure the average apical surface area during ingression, 20-87 NBs from 2-12 embryos of  
560 each genotype were temporally aligned (registered) based on the time when they reached an apical  
561 area of 1.5 to 2.5  $\mu\text{m}^2$ . We did not consider segmentation results below this threshold range. Time  
562 0 (onset of ingression) was defined as the time point at which the average apical surface of  
563 registered cells started declining persistently below  $\sim 40 \mu\text{m}^2$ , which is the average apical cell area  
564 in the ectoderm at the onset of ingression during stage 8 [[Fernandez-Gonzalez and Zallen, 2015](#)].

565 To compare rates of ingression, we matched initial average areas in control and mutant/RNAi  
566 embryos. Ingression speed of individual NBs was the slope of a linear fit (first degree polynomial)  
567 for the apical area loss over time (using the Matlab function *polyfit*). When average fluorescence  
568 results from multiple cells were analyzed, cells were temporally registered using the same area  
569 threshold. For all experiments, we compared controls to mutant or RNAi embryos carrying the  
570 same fluorescent marker(s), and imaged with the same settings and environmental conditions.

571

572 To quantify junctional and medial average protein levels, each cell was divided into two  
573 compartments as described [[Fernandez-Gonzalez and Zallen, 2015](#)]. The junctional compartment

574 was determined by a 3-pixel-wide (0.54  $\mu\text{m}$ ) dilation of the cell outline identified using watershed  
575 or LiveWire segmentation. The medial compartment was obtained by inverting a binary image  
576 representing the junctional compartment. Protein concentrations were quantified as the mean pixel  
577 intensity in each compartment considering either all ingress time points, up to the last 10  
578 minutes of the process (early ingress), or the last 10 minutes (late ingress), as indicated.

579

580 When determining total or average protein intensities, we combined results from different embryos  
581 of the same genetic background/fluorescent marker, imaged with the same confocal settings, and  
582 at the same temperature. Average fluorescence intensities were normalized at each time point by  
583 subtracting the fluorescence mode for the entire image (background) and dividing by the mean  
584 pixel value of each frame. When comparing different genetic backgrounds expressing the same  
585 fluorescent marker (control *versus* mutant or RNAi), average fluorescence intensities at each time  
586 point were normalized by subtracting the fluorescence mode for the entire image (background) at  
587 that time point, on all movie time frames.

588

589 Total Crb and Ecad intensity at each time point were the sum of pixel intensities in the junctional  
590 domain normalized as indicated above. Relative changes in apical cell perimeter and total apical  
591 Crb levels throughout ingress (Fig. 1C and D) were defined as:

592

593  $\Delta\text{perimeter (t)} = (\text{Apical Perimeter (t)} - \text{Apical Perimeter (t-60 sec)}) / \text{Apical Perimeter (t-60 sec)}$

594  $\Delta\text{total Crb levels (t)} = (\text{Total protein (t)} - \text{Total protein (t-60 sec)}) / \text{Total protein (t-60 sec)}$

595

596 To determine fractions of Crb loss or gain during apical oscillations (Figs. 1F, S1A), the apical  
597 perimeter and total fluorescent levels of Crb in individual NBs were smoothed by averaging  
598 over 2 consecutive data points at a temporal resolution of 15 sec. "Peaks" and "troughs" were then  
599 identified from smoothed perimeter values by imposing a minimum separation of 30 seconds  
600 between consecutive peaks and troughs and a perimeter change of at least 1  $\mu\text{m}$ . Contractions were  
601 defined as apical oscillations from consecutive "peaks" to "troughs" and expansions were defined  
602 as apical oscillations from consecutive "troughs" to "peaks". We calculated fractions of perimeter  
603 or Crb change during contractions and expansions as:

604

605  $\text{Fraction\_perimeter\_change\_contraction} = (\text{Perimeter}(\text{peak}) - \text{Perimeter}(\text{trough})) /$

606  $\text{Perimeter}(\text{peak})$

607  $\text{Fraction\_total\_Crb\_change\_contraction} = (\text{Total\_Crb}(\text{peak}) - \text{Total\_Crb}(\text{trough})) /$

608  $\text{Total\_Crb}(\text{peak})$

609  $\text{Fraction\_perimeter\_change\_expansion} = (\text{Perimeter}(\text{trough}) - \text{Perimeter}(\text{peak})) /$

610  $\text{Perimeter}(\text{trough})$

611  $\text{Fraction\_total\_Crb\_change\_expansion} = (\text{Total\_Crb}(\text{trough}) - \text{Total\_Crb}(\text{peak})) /$

612  $\text{Total\_Crb}(\text{trough})$

613

614 Rate of apical area change,  $\Delta\text{Area}(t)$ , was defined as  $\Delta\text{Area}(t) = \text{Area}(t) - \text{Area}(t-60 \text{ seconds})$ ,

615 whereas rate of medial or junctional myosin II change was defined as  $\Delta\text{myosin}(t) = \text{myosin}$

616  $\text{concentration}(t) - \text{myosin concentration}(t-60 \text{ seconds})$ . The duration of apical contractions and

617 expansions was defined as the number of consecutive time points multiplied by time resolution

618 during which  $\Delta\text{Area}(t)$  was  $<0$  or  $>0$ , respectively. The amplitude of contractions and expansions

619 was the maximum value of area change within each event.

620

621 To quantify FM4-64 internalization in live NBs and NICs, we quantified the average FM4-64

622 fluorescence in the medial cell compartment throughout time after injection (images acquired at 4

623 seconds intervals). The image intensity mode (background) was subtracted at each time point, and

624 the result divided by the image intensity mean at each time point. Fluorescence intensities were

625 then normalized to the first time point of movie acquisition, in order to compare the relative

626 internalization of FM4-64 in ingressing NBs versus NICs.

627

628 To determine total levels of internalized Crb in fixed NBs, we employed LiveWire in Siesta and

629 segmented the membrane outline of NBs at individual Z planes (Z step size = 0.37  $\mu\text{m}$ )

630 encompassing the entire apical-basal height of the cell. Total intracellular Crb levels were the sum

631 of total fluorescence intensity in the medial compartment for all Z planes encompassing that cell.

632 Fluorescence intensities were normalized by subtracting the fluorescence mode at each Z plane.

633 The size of Crb containing endosomes in NBs and non-ingressing cells was determined in Fiji

634 using Watershed Segmentation and Analyze Particles in manually drawn ROI around cells of

635 interest. Original images in the Crb channel were converted to binary images via thresholding

636 (default method in Fiji); only segmented vesicles with a larger size than 10 pixels (1 pixel=60.13  
637 nm) were considered for analysis. Data was obtained from wild-type embryos using fixation  
638 Method B (see above).

639

640 For colocalization analysis between internalized Crb and several endocytic/cytoskeletal/polarity  
641 markers (Figs. 4B,D and S3), we used Coloc2 (Fiji) in manually drawn ROIs around NBs of fixed  
642 embryos, in order to obtain Pearson's coefficients and Mander's coefficients. We employed the  
643 Costes method [Costes et al., 2004] to assess the significance of the calculated Mander's co-  
644 localization coefficients, by analysing 200 image randomizations in the Crb channel for each cell,  
645 considering a point spread function (PSF) of 3 pixels (1 pixel = 60.13 nm).

646

#### 647 **Statistics**

648 Average or median values were determined based on a certain number, n, of embryos/cells/  
649 /contractions/expansions, as indicated in each figure legend. Error bars are SD (standard deviation)  
650 or SEM (standard error of the mean), which is  $SD/\sqrt{n}$  or interquartile ranges, as indicated. We used  
651 Graphpad Prism 8 to test if the n values of each sample followed a normal distribution, by  
652 performing a D'Agostino and Pearson normality test. We employed unpaired 2-tailed T tests to  
653 determine p values when samples passed the normality test and non-parametric 2 sample  
654 Kolmogorov Smirnov (KS) or Mann-Whitney tests otherwise. F-test was used to assess the  
655 variance between two samples.

656

657

658 **Acknowledgements**

659 We thanks Francois Schweisguth, Hugo Bellen, Yang Hong, Chris Doe, Elisabeth Knust, Adam  
660 Martin, Eric Wieschaus, Jennifer Zallen, Hiroki Oda, Thomas Lecuit, Daniel St. Johnston, the  
661 Bloomington Drosophila Stock Center, the Drosophila RNAi Screening Center at Harvard Medical  
662 School, and the Developmental Studies Hybridoma Bank for reagents. We like to thank Dorothea  
663 Godt for critical reading of the manuscript, and the Imaging Facility of the Department of Cell and  
664 Systems Biology, University of Toronto, for support. **Funding:** This work was funded by an  
665 Innovation Grant from the Canadian Cancer Society (to U.T. and R.F.G.) and a project grant from  
666 the Canadian Institutes for Health Research (to U.T. and R.F.G.). R.F.G. is a Canada Research  
667 Chair in Quantitative Cell Biology and Morphogenesis and U.T. is a Canada Research Chair for  
668 Epithelial Polarity and Development.

669

670 **Author contributions**

671 The project was conceived and experiments were designed by S.S. and U.T. S.S. did the majority  
672 of the experimental work and data analysis. G.L., M.P., D.t.S, and K.A.K. contributed to the  
673 experimental work. G.L. P.G., T.L., and D.K. contributed to data analysis. J.Y. and R.F.G.  
674 generated code and contributed expertise in data analysis. R.F.G and U.T. provided supervision  
675 and raised funds. The paper was written by S.S. and U.T.

676

677 **Competing interest**

678 The authors declare no competing interests.

679

680 **Data and material availability**

681 All data are available in the manuscript or supplementary materials.

682

683 **Supplementary materials**

684 Materials and Methods

685 Supplemental Figures S1 – S5

686 Supplemental Videos 1 – 10

687

688 **References**

- 689
- 690 An Y, Xue G, Shaobo Y, Mingxi D, Zhou X, Yu W, Ishibashi T, Zhang L, Yan Y. Apical constriction is  
691 driven by a pulsatile apical myosin network in delaminating *Drosophila* neuroblasts. *Development*  
692 **144**, 2153-2164. (2017) doi: 10.1242/dev.150763.
- 693 Arefin B, Parvin F, Bahrampour S, Stadler CB, Thor S. *Drosophila* Neuroblast Selection Is Gated by  
694 Notch, Snail, SoxB, and EMT Gene Interplay. *Cell Rep.* **29**, 3636-3651.e3. (2019). doi:  
695 10.1016/j.celrep.2019.11.038.
- 696 Bachmann, A., Schneider, M., Theilenberg, E., Grawe, F. & Knust, E. *Drosophila* Stardust is a partner of  
697 Crumbs in the control of epithelial cell polarity. *Nature* **414**, 638-643, (2001).  
698 doi:10.1038/414638a.
- 699 Boulianne GL, de la Concha A, Campos-Ortega JA, Jan LY, Jan YN. The *Drosophila* neurogenic gene  
700 neuralized encodes a novel protein and is expressed in precursors of larval and adult neurons.  
701 *EMBO J.* **10**, 2975-83. (1991).
- 702 Bulgakova NA, Rentsch M, Knust E. Antagonistic functions of two stardust isoforms in *Drosophila*  
703 photoreceptor cells. *Mol Biol Cell.* **21**, 3915-25. (2010). doi: 10.1091/mbc.E09-10-0917.
- 704 Campbell K, Whissell G, Franch-Marro X, Batlle E, Casanova J. Specific GATA factors act as conserved  
705 inducers of an endodermal-EMT. *Dev Cell.* **21**, 1051-61. (2011). doi:  
706 10.1016/j.devcel.2011.10.005.
- 707 Campbell K. Contribution of epithelial-mesenchymal transitions to organogenesis and cancer metastasis.  
708 *Curr Opin Cell Biol.* **55**, 30-35. (2018). doi: 10.1016/j.ceb.2018.06.008. Epub 2018 Jul 11.
- 709 Cavanaugh KE, Staddon MF, Munro E, Banerjee S, Gardel ML. RhoA Mediates Epithelial Cell Shape  
710 Changes via Mechanosensitive Endocytosis. *Dev Cell.* **52**, 152-166. (2020). doi:  
711 10.1016/j.devcel.2019.12.002.
- 712 Chanet S, Schweisguth F. Regulation of epithelial polarity by the E3 ubiquitin ligase Neuralized and the  
713 Bearded inhibitors in *Drosophila*. *Nat Cell Biol.* **14**, 467-76. (2012). doi: 10.1038/ncb2481.
- 714 Chou, T. B. & Perrimon, N. The autosomal FLP-DFS technique for generating germline mosaics in  
715 *Drosophila melanogaster*. *Genetics* **144**, 1673-1679 (1996).
- 716 Corson, F., Couturier, L., Rouault, H., Mazouni, K. & Schweisguth, F. Self-organized Notch dynamics  
717 generate stereotyped sensory organ patterns in *Drosophila*. *Science* **356**, eaai7407. (2017).  
718 doi:10.1126/science.aai7407.
- 719 Costes, S. V. *et al.* Automatic and quantitative measurement of protein-protein colocalization in live cells.  
720 *Biophys J* **86**, 3993-4003. (2004). doi:10.1529/biophysj.103.038422.
- 721 Dongre A, Weinberg RA. New insights into the mechanisms of epithelial-mesenchymal transition and  
722 implications for cancer. *Nat Rev Mol Cell Biol.* **20**, 69-84. (2019). doi: 10.1038/s41580-018-  
723 0080-4.
- 724 Fernandez-Gonzalez, R. & Zallen, J. A. Oscillatory behaviors and hierarchical assembly of contractile  
725 structures in intercalating cells. *Phys Biol* **8**, 045005. (2011). doi:10.1088/1478-3975/8/4/045005.
- 726 Fernandez-Gonzalez, R. & Zallen, J. A. Wounded cells drive rapid epidermal repair in the early  
727 *Drosophila* embryo. *Mol Biol Cell* **24**, 3227-3237. (2013). doi:10.1091/mbc.E13-05-0228.
- 728 Gamblin CL, Hardy ÉJ, Chartier FJ, Bisson N, Laprise P. A bidirectional antagonism between aPKC and  
729 Yurt regulates epithelial cell polarity. *J Cell Biol.* **204**, 487-95. (2014) doi:  
730 10.1083/jcb.201308032.
- 731 Garcia De Las Bayonas A, Philippe JM, Lellouch AC, Lecuit T. Distinct RhoGEFs Activate Apical and  
732 Junctional Contractility under Control of G Proteins during Epithelial Morphogenesis. *Curr Biol.*  
733 **29**; 3370-3385.e7. (2019). doi: 10.1016/j.cub.2019.08.017.
- 734 Gheisari E, Aakhte M, Müller HJ. Gastrulation in *Drosophila melanogaster*: Genetic control, cellular  
735 basis and biomechanics. *Mech Dev.* **163**, 103629. (2020) doi: 10.1016/j.mod.2020.103629. Epub  
736 2020 Jun 29.
- 737 Grawe F, Wodarz A, Lee B, Knust E, Skaer H. The *Drosophila* genes crumbs and stardust are involved in  
738 the biogenesis of adherens junctions. *Development* **122**, 951-9. (1996).



- 739 Haglund K, Dikic I. The role of ubiquitylation in receptor endocytosis and endosomal sorting. *J Cell Sci.*  
740 **125**, 265-75. (2012). doi: 10.1242/jcs.091280.
- 741 Hartenstein V, Wodarz A. Initial neurogenesis in Drosophila. *Wiley Interdiscip Rev Dev Biol.* **2**, 701-21.  
742 (2013). doi: 10.1002/wdev.111.
- 743 Hay ED. An overview of epithelio-mesenchymal transformation. *Acta Anat.* **154**, 8-20. (1995). doi:  
744 10.1159/000147748.
- 745 Hirono, K., Margolis, J. S., Posakony, J. W. & Doe, C. Q. Identification of hunchback cis-regulatory  
746 DNA conferring temporal expression in neuroblasts and neurons. *Gene Expr Patterns* **12**, 11-17.  
747 (2012). doi:10.1016/j.gexp.2011.10.001.
- 748 Huang, J., Zhou, W., Dong, W., Watson, A. M. & Hong, Y. From the Cover: Directed, efficient, and  
749 versatile modifications of the Drosophila genome by genomic engineering. *Proc Natl Acad Sci U*  
750 *S A* **106**, 8284-8289. (2009). doi:10.1073/pnas.0900641106.
- 751 Jung HY, Fattet L, Tsai JH, Kajimoto T, Chang Q, Newton AC, Yang J. Apical-basal polarity inhibits  
752 epithelial-mesenchymal transition and tumour metastasis by PAR-complex-mediated SNAIL  
753 degradation. *Nat Cell Biol.* **21**, 359-371. (2019). doi: 10.1038/s41556-019-0291-8.
- 754 Kovall RA, Gebelein B, Sprinzak D, Kopan R. The Canonical Notch Signaling Pathway: Structural and  
755 Biochemical Insights into Shape, Sugar, and Force. *Dev Cell.* **41**, 228-241. (2017). doi:  
756 10.1016/j.devcel.2017.04.001.
- 757 Lambert AW, Weinberg RA. Linking EMT programmes to normal and neoplastic epithelial stem cells.  
758 *Nat Rev Cancer.* **21**, 325-338. (2021). doi: 10.1038/s41568-021-00332-6. Epub 2021 Feb 5.
- 759 Lamouille S, Xu J, Derynck R. Molecular mechanisms of epithelial-mesenchymal transition. *Nat Rev Mol*  
760 *Cell Biol.* **15**, 178-96. (2014). doi: 10.1038/nrm3758.
- 761 Leung, C. Y. & Fernandez-Gonzalez, R. Quantitative image analysis of cell behavior and molecular  
762 dynamics during tissue morphogenesis. *Methods Mol Biol* **1189**, 99-113. (2015).  
763 doi:10.1007/978-1-4939-1164-6\_7.
- 764 Lim J, Thiery JP. Epithelial-mesenchymal transitions: insights from development. *Development* **139**,  
765 3471-86. (2012). doi: 10.1242/dev.071209.
- 766 Lin YH, Currinn H, Pocha SM, Rothnie A, Wassmer T, Knust E. AP-2-complex-mediated endocytosis of  
767 Drosophila Crumbs regulates polarity by antagonizing Stardust. *J Cell Sci.* **128**, 4538-49. (2015).  
768 doi: 10.1242/jcs.174573.
- 769 Martin, A. C., Gelbart, M., Fernandez-Gonzalez, R., Kaschube, M. & Wieschaus, E. F. Integration of  
770 contractile forces during tissue invagination. *J Cell Biol.* **188**, 735-749. (2010).  
771 doi:10.1083/jcb.200910099.
- 772 Martin, A. C., Kaschube, M. & Wieschaus, E. F. Pulsed contractions of an actin-myosin network drive  
773 apical constriction. *Nature* **457**, 495-499. (2009). doi:10.1038/nature07522.
- 774 McNally KE, Cullen PJ. Endosomal Retrieval of Cargo: Retromer Is Not Alone. *Trends Cell Biol.* **28**,  
775 807-822. (2018). doi: 10.1016/j.tcb.2018.06.005.
- 776 Mettlen M, Chen PH, Srinivasan S, Danuser G, Schmid SL. Regulation of Clathrin-Mediated  
777 Endocytosis. *Annu Rev Biochem.* **87**, 871-896. (2018) doi: 10.1146/annurev-biochem-062917-  
778 012644.
- 779 Médina E, Williams J, Klipfell E, Zarnescu D, Thomas G, Le Bivic A. Crumbs interacts with moesin and  
780 beta(Heavy)-spectrin in the apical membrane skeleton of Drosophila. *J Cell Biol.* **158**, 941-51.  
781 (2002). doi: 10.1083/jcb.200203080.
- 782 Miller SW, Posakony JW. Lateral inhibition: Two modes of non-autonomous negative autoregulation by  
783 neuralized. *PLoS Genet.* **14**, e1007528. (2018). doi: 10.1371/journal.pgen.1007528.
- 784 Morais-de-Sá E, Mirouse V, St Johnston D. aPKC phosphorylation of Bazooka defines the apical/lateral  
785 border in Drosophila epithelial cells. *Cell* **141**, 509-23. (2010) doi: 10.1016/j.cell.2010.02.040.
- 786 Nieto MA, Huang RY, Jackson RA, Thiery JP. EMT: 2016. *Cell* **166**, 21-45. (2016). doi:  
787 10.1016/j.cell.2016.06.028.

- 788 Oda, H. & Tsukita, S. Real-time imaging of cell-cell adherens junctions reveals that Drosophila  
789 mesoderm invagination begins with two phases of apical constriction of cells. *J Cell Sci* **114**, 493-  
790 501 (2001).
- 791 Ozdamar B, Bose R, Barrios-Rodiles M, Wang HR, Zhang Y, Wrana JL. Regulation of the polarity  
792 protein Par6 by TGFbeta receptors controls epithelial cell plasticity. *Science* **307**, 1603-9. (2005).  
793 doi: 10.1126/science.1105718. PMID: 15761148
- 794 Pellikka M, Tanentzapf G, Pinto M, Smith C, McGlade CJ, Ready DF, Tepass U. Crumbs, the Drosophila  
795 homologue of human CRB1/RP12, is essential for photoreceptor morphogenesis. *Nature* **416**,  
796 143-149. (2002). doi:10.1038/nature721.
- 797 Perez-Mockus G, Mazouni K, Roca V, Corradi G, Conte V, Schweisguth F. Spatial regulation of  
798 contractility by Neuralized and Bearded during furrow invagination in Drosophila. *Nat Commun.*  
799 **8**, 1594. (2017b). doi: 10.1038/s41467-017-01482-8.
- 800 Perez-Mockus G, Roca V, Mazouni K, Schweisguth F. Neuralized regulates Crumbs endocytosis and  
801 epithelium morphogenesis via specific Stardust isoforms. *J Cell Biol.* **216**, 1405-1420. (2017a).  
802 doi: 10.1083/jcb.201611196.
- 803 Perez-Mockus G, Schweisguth F. Cell Polarity and Notch Signaling: Linked by the E3 Ubiquitin Ligase  
804 Neuralized? *Bioessays* **39**. (2017). doi: 10.1002/bies.201700128.
- 805 Petronczki, M. & Knoblich, J. A. DmPAR-6 directs epithelial polarity and asymmetric cell division of  
806 neuroblasts in Drosophila. *Nat Cell Biol* **3**, 43-49. (2001). doi:10.1038/35050550.
- 807 Pfeiffer, B. D., Truman, J. W. & Rubin, G. M. Using translational enhancers to increase transgene  
808 expression in Drosophila. *Proc Natl Acad Sci U S A* **109**, 6626-6631. (2012).  
809 doi:10.1073/pnas.1204520109.
- 810 Pichaud F, Walther RF, Nunes de Almeida F. Regulation of Cdc42 and its effectors in  
811 epithelia24morphogenesis. *J Cell Sci.* **132**, jcs217869. (2019). doi: 10.1242/jcs.217869.
- 812 Pickett MA, Nature VF, Feldman JL. A Polarizing Issue: Diversity in the Mechanisms Underlying  
813 Apico-Basolateral Polarization In Vivo. *Annu Rev Cell Dev Biol.* **35**, 285-308. (2019). doi:  
814 10.1146/annurev-cellbio-100818-125134.
- 815 Pocha SM, Wassmer T, Niehage C, Hoflack B, Knust E. Retromer controls epithelial cell polarity by  
816 trafficking the apical determinant Crumbs. *Curr Biol.* **21**, 1111-7. (2011). doi:  
817 10.1016/j.cub.2011.05.007.
- 818 Ramkumar N, Omelchenko T, Silva-Gagliardi NF, McGlade CJ, Wijnholds J, Anderson KV. Crumbs2  
819 promotes cell ingression during the epithelial-to-mesenchymal transition at gastrulation. *Nat Cell*  
820 *Biol.* **18**, 1281-1291. (2016). doi: 10.1038/ncb3442.
- 821 Rigal A, Doyle SM, Robert S. Live cell imaging of FM4-64, a tool for tracing the endocytic pathways in  
822 Arabidopsis root cells. *Methods Mol Biol.* **1242**, 93-103. (2015). doi: 10.1007/978-1-4939-1902-  
823 4\_9.
- 824 Rodriguez-Boulan E, Macara IG. Organization and execution of the epithelial polarity programme. *Nat*  
825 *Rev Mol Cell Biol.* **15**, 225-42. (2014) doi: 10.1038/nrm3775.
- 826 Serrano Nájera G, Weijer CJ. Cellular processes driving gastrulation in the avian embryo. *Mech Dev.* **163**,  
827 103624. (2020). doi: 10.1016/j.mod.2020.103624.
- 828 Shard C, Luna-Escalante J, Schweisguth F. Tissue-wide coordination of epithelium-to-neural stem cell  
829 transition in the Drosophila optic lobe requires Neuralized. *J Cell Biol.* **219**, e202005035. (2020).  
830 doi: 10.1083/jcb.202005035. PMID: 32946560
- 831 Sheng G. Defining epithelial-mesenchymal transitions in animal development. *Development.* **148**,  
832 dev198036. (2021). doi: 10.1242/dev.198036. Epub 2021 Apr 20. PMID: 33913481
- 833 Shook D, Keller R. Mechanisms, mechanics and function of epithelial-mesenchymal transitions in early  
834 development. *Mech Dev.* **120**, 1351-83. (2003). doi: 10.1016/j.mod.2003.06.005. PMID:  
835 14623443
- 836 Silver JT, Wirtz-Peitz F, Simões S, Pellikka M, Yan D, Binari R, Nishimura T, Li Y, Harris TJC,  
837 Perrimon N, Tepass U. Apical polarity proteins recruit the RhoGEF Cysts to promote junctional  
838 myosin assembly. *J Cell Biol.* **218**, 3397-3414. (2019). doi: 10.1083/jcb.201807106.

- 839 Simões S, Oh Y, Wang MFZ, Fernandez-Gonzalez R, Tepass U. Myosin II promotes the anisotropic loss  
840 of the apical domain during *Drosophila* neuroblast ingression. *J Cell Biol.* **216**, 1387-1404.  
841 (2017) doi: 10.1083/jcb.201608038.
- 842 Tepass U, Gruszynski-DeFeo E, Haag TA, Omatyar L, Török T, Hartenstein V. shotgun encodes  
843 *Drosophila* E-cadherin and is preferentially required during cell rearrangement in the  
844 neurectoderm and other morphogenetically active epithelia. *Genes Dev.* **10**, 672-85. (1996). doi:  
845 10.1101/gad.10.6.672.
- 846 Tepass U, Knust E. Crumbs and stardust act in a genetic pathway that controls the organization of  
847 epithelia in *Drosophila melanogaster*. *Dev Biol.* **159**, 311-26. (1993). doi:  
848 10.1006/dbio.1993.1243.
- 849 Tepass U, Theres C, Knust E. *crumbs* encodes an EGF-like protein expressed on apical membranes of  
850 *Drosophila* epithelial cells and required for organization of epithelia. *Cell* **61**, 787-99. (1990). doi:  
851 10.1016/0092-8674(90)90189-1.
- 852 Tepass U. Crumbs, a component of the apical membrane, is required for zonula adherens formation in  
853 primary epithelia of *Drosophila*. *Dev Biol.* **177**, 217-25. 1996 doi: 10.1006/dbio.1996.0157.
- 854 Tepass U. The apical polarity protein network in *Drosophila* epithelial cells: regulation of polarity,  
855 junctions, morphogenesis, cell growth, and survival. *Annu Rev Cell Dev Biol.* **28**, 655-85. (2012).  
856 doi: 10.1146/annurev-cellbio-092910-154033.
- 857 Vietri M, Radulovic M, Stenmark H. The many functions of ESCRTs. *Nat Rev Mol Cell Biol.* **21**, 25-42.  
858 (2020). doi: 10.1038/s41580-019-0177-4.
- 859 Wang S, Tan KL, Agosto MA, Xiong B, Yamamoto S, Sandoval H, Jaiswal M, Bayat V, Zhang K,  
860 Charng WL, David G, Duraine L, Venkatachalam K, Wensel TG, Bellen HJ. The retromer  
861 complex is required for rhodopsin recycling and its loss leads to photoreceptor degeneration.  
862 *PLoS Biol.* **12**, e1001847. (2014). doi: 10.1371/journal.pbio.1001847.
- 863 Wodarz A, Hinz U, Engelbert M, Knust E. Expression of crumbs confers apical character on plasma  
864 membrane domains of ectodermal epithelia of *Drosophila*. *Cell* **82**, 67-76. (1995). doi:  
865 10.1016/0092-8674(95)90053-5.
- 866 Yang J, Antin P, Berx G, Blanpain C, Brabletz T, Bronner M, Campbell K, Cano A, Casanova J,  
867 Christofori G, Dedhar S, Derynck R, Ford HL, Fuxe J, García de Herreros A, Goodall GJ,  
868 Hadjantonakis AK, Huang RJY, Kalchauer C, Kalluri R, Kang Y, Khew-Goodall Y, Levine H,  
869 Liu J, Longmore GD, Mani SA, Massagué J, Mayor R, McClay D, Mostov KE, Newgreen DF,  
870 Nieto MA, Puisieux A, Runyan R, Savagner P, Stanger B, Stemmler MP, Takahashi Y, Takeichi  
871 M, Theveneau E, Thiery JP, Thompson EW, Weinberg RA, Williams ED, Xing J, Zhou BP,  
872 Sheng G; EMT International Association (TEMTIA). Guidelines and definitions for research on  
873 epithelial-mesenchymal transition. *Nat Rev Mol Cell Biol.* **21**, 341-352. (2020) doi:  
874 10.1038/s41580-020-0237-9.
- 875 Zhou B, Wu Y, Lin X. Retromer regulates apical-basal polarity through recycling Crumbs. *Dev Biol.* **360**,  
876 87-95. (2011). doi: 10.1016/j.ydbio.2011.09.009.
- 877

878 **Figure legends**

879

880 **Figure 1. Crb persists during early NB ingress and undergoes rapid removal during late**  
881 **ingression.**

882 (A) Schematic of gastrulating *Drosophila* embryo (stage 8) when S1 NBs ingress. NICs, non-ingressing  
883 cells.

884 (B) Apical surface of ingressing live NBs (yellow dots or arrowheads) expressing endo-Crb::GFP or  
885 endo-Ecad::GFP. Time after onset of ingress. Scale bars, 5  $\mu\text{m}$ .

886 (C-D) Junctional Crb::GFP and Ecad::GFP fluorescence (average pixel intensity at cell boundaries; C)  
887 and total apical protein levels (fluorescence intensity per cell; D). Blue lines represent average apical area.  
888 58 NBs, 12 embryos for endo-Crb::GFP and 30 NBs, 6 embryos for endo-Ecad::GFP. T=0 min, the onset  
889 of ingress. Error bars are SEM.

890 (E) Apical perimeter and total apical Crb::GFP during ingress (upper panel; T=0 min, onset of  
891 ingress) and fraction of change in apical perimeter and total Crb::GFP during ingress of a  
892 representative NB. Apical Crb levels decrease (rate <0) during apical contractions and increase (rate >0)  
893 during apical expansions. Apical Crb losses overtake gains during late ingress.

894 (F) Scatter plot showing the relationship between the fraction of perimeter change during apical  
895 contractions or expansions and the corresponding fraction of total apical Crb change (relative Crb  
896 increase or decrease). N values as in Fig. S1A.

897 (G) Schematic interpretation of data in (F) illustrating preferential Crb membrane removal during cell  
898 contraction and re-insertion during apical surface expansion.

899

900 **Figure 2. Crb overexpression delays NB ingress.**

901 (A) Ingressing live NBs (arrowheads) expressing endo-Ecad::GFP and sqh-Sqh::mCherry in H<sub>2</sub>O injected  
902 (control) and Crb overexpression (OE) embryos. T=0 min, onset of ingress. Scale bars, 5  $\mu\text{m}$ .

903 (B) NB ingress speed in Crb-OE (51 NBs, 10 embryos) and controls (48 NBs, 6 embryos). Median  
904 values: -1.35 (control), -1.0 (Crb-OE), KS test: \*  $p=2.5 \times 10^{-2}$ ; F-test (to test for differences in variance of  
905 ingress speed): ns (not significant),  $p=0.07$ ; Bars are IQRs.

906 (C) Apical area loss of NBs is slowed in Crb OE embryos. Control (blue line; 20 NBs, 2 embryos, 159  
907 time points spaced by 10 sec) versus Crb OE (green line; 26 NBs, 5 embryos, 220 time points spaced by  
908 10 sec).

909 (D) Amplitude and duration of apical contractions and expansions of NB in Crb OE embryos (26 NBs, 5  
910 embryos) versus controls (20 NBs, 2 embryos). Median amplitudes of expansions for control/Crb OE,  
911 1.17/1.84  $\mu\text{m}^2/\text{min}$ ; \*\*\*\*,  $p=5 \times 10^{-4}$ ; and contractions, 2.76/3.04  $\mu\text{m}^2/\text{min}$ ; ns,  $p=0.43$ . Median durations

912 of expansions for control/Crb OE, 17.39/18.87 sec; \*,  $p=0.01$ ; and contractions, 48.64/33.06 sec, \*\*,  $p$   
913  $=1 \times 10^{-3}$  (KS test); 241–566 events per condition.

914 (E) Ventral ectoderm in late stage 8 control and Crb OE embryos, stained for Crb (red) and Ecad (green).  
915 Apical is up. Note ectopic Crb on the lateral cell membrane in Crb OE cells and loss of apical Ecad  
916 signal. Scale bars, 5  $\mu\text{m}$ . Quantification of Ecad levels in ingressing NBs. N values as in (D). \*\*\*\*  
917  $p=9.6 \times 10^{-67}$  (2-tailed T test; mean  $\pm$  SD).

918 (F) Myosin levels in NBs of Crb OE embryos. Schematic of junctional and medial myosin pools in the  
919 apical domain of ingressing NBs. Crb OE reduces junctional myosin and enhances medial myosin. N  
920 values as in (D). \*\*\*\*,  $p=8.2 \times 10^{-136}$ ,  $8.2 \times 10^{-38}$  (2-tailed T test; means  $\pm$  SD).

921 (G) Representative plots showing the rate of medial myosin change (a.u./min) during ingression in a  
922 control and a Crb OE NB. Positive rates indicate medial myosin assembly; negative rates indicate  
923 disassembly. T=0 min, onset of ingression.

924 (H) Medial myosin assembly and disassembly rates (Amplitude) during ingression. Duration indicates  
925 total time medial myosin spent increasing/assembling or decreasing/disassembling. N values as in (D).  
926 Median rates of medial myosin change of control/Crb OE for assembly, 0.07/0.1 a.u./min; \*\*\*,  
927  $p=3.0 \times 10^{-4}$ ; and disassembly, 0.06/0.08 a.u./min; \*\*,  $p=2.6 \times 10^{-3}$ . Median durations for control/Crb OE  
928 for assembly, 24/28 sec; \*\*\*,  $p=1 \times 10^{-3}$ ; and disassembly, 18/28 sec, \*\*\*\*,  $p=7.9 \times 10^{-6}$  (KS test); 328–  
929 553 events per condition.

930

931 **Figure 3. Crb and the RhoGEF Cysts are required for normal NB ingression dynamics**

932 (A) Mean apical area loss during NB ingression in *crb* dsRNA injected embryos. T=0 min, onset of  
933 ingression. Means  $\pm$  SEM. Control: 20 NBs, 3 embryos, 260 time points spaced by 6 sec, *crb*-RNAi: 38  
934 NBs, 5 embryos, 176 time points spaced by 6 sec.

935 (B) NB ingression speed in *crb*-RNAi (n=91 NBs, 12 embryos), *cyst*-RNAi (21 NBs, 3 embryos), and  
936 control embryos (68 NBs, 10 embryos; 19 NBs, 4 embryos, respectively). Median values: -1.5 (H<sub>2</sub>O  
937 injected), -1.6 (*crb*-RNAi), -1.6 (*cysts*-RNAi control), -2.6 (*cysts*-RNAi). KS tests: ns,  $p=0.09$ , \*\*  
938  $p=0.0014$ ; F-tests (to test for differences in variance of ingression speed): \*\*\*\*  $p=1.7 \times 10^{-5}$ ; ns,  $p=0.23$ .  
939 Bars are IQRs.

940 (C) Mean apical area loss, the 10 fastest and the 10 slowest ingressing NBs in *crb*-RNAi (5 embryos;  
941 control, H<sub>2</sub>O injected, 20 NBs, 3 embryos). T=0 min, time point when the average apical surface of each  
942 ingressing cell population was 22  $\mu\text{m}^2$ . Means  $\pm$  SEM.

943 (D-E) Junctional and medial myosin levels (D, \*\*\*\*,  $p=2.5 \times 10^{-85}$ ;  $3.4 \times 10^{-19}$ ;) and Ecad (E, \*\*\*\*  
944  $p=1.1 \times 10^{-40}$ ) in ingressing NBs from *crb* dsRNA injected and H<sub>2</sub>O-injected embryos. N values as in (B).  
945 (2-tailed T test). Means  $\pm$  SD.

946 (F) Cysts is one of several Crb complex (Crb/Sdt) effectors. Cysts stimulates Rho1 to enhance junctional  
947 myosin II. Other Crb/Sdt effectors are the Par6/aPKC complex which undergoes negative feedback  
948 regulation with basolateral polarity proteins (Scrib/Dlg/Lgl and Yurt/Cora), and Moesin and  $\beta$ <sub>H</sub>-Spectrin  
949 which support apical membrane stability [Tepass, 2012; Silver et al., 2019].

950 (G) Mean apical area loss during NB ingression in *cysts*-RNAi embryos compared to best-match controls.  
951 T=0 min indicates the onset of ingression. Data presented are means +/- SEM. N values: control (19 NBs,  
952 4 embryos, 97 time points spaced by 15 sec) versus *cysts*-RNAi (21 NBs, 3 embryos, 59 time points  
953 spaced by 15 sec).

954

#### 955 **Figure 4. Crb endocytosis facilitates NB ingression.**

956 (A) In late ingressing NBs, Crb is found at the apical membrane (apical, arrowheads) and in large  
957 endosomes 0.9  $\mu$ m below the apical surface (basal, arrowheads). After ingression, Crb is seen in large  
958 endosomes in the perinuclear region. Arrowheads in apical sections point to the position of NBs prior to  
959 ingression. Arrowheads in the basal sections point to NBs 6  $\mu$ m below the surface. Yurt labels the  
960 basolateral membrane. Scale bars, 5  $\mu$ m.

961 (B) Single ingressed NBs displaying co-localization of Crb and the endosome markers Hrs, Vps26, Delta,  
962 and Ecad. The plasma membrane is labelled with Discs Large (Dlg). Scale bars, 2.5  $\mu$ m.

963 (C) Frequency of Crb-positive endosomes in NBs after ingression versus adjacent non-ingressing cells  
964 (NICs) according to endosomal size. Ingressed NBs contain larger Crb-positive endosomes than NICs.  
965 N=2024 endosomes from 84 NBs and 751 endosomes from 77 NICs (5 embryos).

966 (D) Mander's and Pearson's co-localization coefficients (M/PCC) of intracellular Crb and markers shown  
967 in (B) in ingressed NBs. See Fig. S3 for positive and negative co-localization controls. 67-109 NBs from  
968 3-7 embryos analyzed per condition.

969 (E) Stills from time-lapse movies of ingressing NBs expressing GFP::Crb (control) or GFP::CrbRR (dots  
970 and arrowheads). Control NBs lost their apical domain within ~35 min (35 NBs, 6 embryos);  
971 GFP::CrbRR expression strongly delayed ingression: 75% of NBs completed ingression after ~70 min  
972 (middle panels; 55 NBs, 6 embryos) and 25% divided on the embryo surface (lower panels; 18 NBs, 6  
973 embryos). Note NBs at 40 minutes showing mitotic rounding. Scale bar, 5  $\mu$ m.

974 (F) NBs at stage 9 expressing GFP::Crb (84 NBs, 4 embryos) or GFP::CrbRR (115 NBs, 7 embryos) in  
975 the absence of endogenous Crb (*crb*<sup>1a22</sup> mutant embryos). GFP::CrbRR is mostly retained cortically  
976 (95/115 NBs), while GFP::Crb localizes to endosomes (84/84 NBs). Scale bar, 5  $\mu$ m.

977 (G) Total GFP::Crb and GFP::CrbRR fluorescence levels at the junctional domain during ingression. N  
978 values as in (F). Means +/- SEM.

979 **(H)** Mean apical area loss during ingression in GFP::Crb (35 NB, 6 embryos) or GFP::CrbRR (55 NBs, 6  
980 embryos) expressing NBs. T=0 min indicates the onset of ingression. Data presented are means +/- SEM.  
981 **(I,J)** Duration and amplitude of individual apical contractions/expansions during ingression in GFP::Crb  
982 versus GFP::CrbRR expressing NBs. Median duration for GFP::Crb/GFP::CrbRR of contractions,  
983 64.1/54.6 sec, \*\*\*,  $p=1 \times 10^{-4}$ ; expansions, 34/33.6 sec, ns (not significant),  $p=0.51$  (KS test); Median  
984 amplitudes for GFP::Crb/GFP::CrbRR (of contractions, 3.2/2.6  $\mu\text{m}^2/\text{min}$ ; \*\*,  $p=1 \times 10^{-3}$ ; expansions,  
985 1.7/1.8  $\mu\text{m}^2/\text{min}$ ; ns,  $p=0.94$  (KS test);  $n=514-1553$  events per condition.

986

987 **Figure 5. Upregulation of endocytic regulators and apical membrane internalization during NB**  
988 **ingression.**

989 **(A-B)** NBs increase apical endocytosis. Ingressing live NB (cell in the center; A) after injection of the  
990 lipophilic, non-cell permeable fluorescent dye FM4-64 at 8 mM, which marks the plasma membrane and  
991 apical vesicles (endosomes). Scale bar, 5  $\mu\text{m}$ . (B) Intracellular FM4-64 in late ingressing NBs (14 NBs, 4  
992 embryos) and temporally matched non-ingressing cells (NICs; 14 cells from 4 embryos), normalized to  
993 the initial time point of movie recording (~2 minutes after injection of the dye into the perivitelline space  
994 of the embryo). The initial mean apical area of NBs at T=0 min was ~19  $\mu\text{m}^2$ . Over the course of 6  
995 minutes, the average fluorescence of internalized FM4-64 increased in ingressing NBs and kept constant  
996 in NICs. T=0 min, start of video recording. Means +/- SEM.

997 **(C-F)** Ingressing live NB co-expressing Dynamin::GFP and GAP43::mCherry (C,D) or Clathrin::GFP  
998 and GAP43::mCherry (E-F) Dots/arrowheads indicate the NB apical domain. T=0 min, onset of  
999 ingression. Scale bar, 5  $\mu\text{m}$ . Normalized fluorescence intensity during early and late ingression.

1000 Individual dots are averages of protein levels at the cell junctions of 13 temporally registered ingressing  
1001 NBs from 2 embryos (D) or 31 temporally registered ingressing NBs from 7 embryos (F). Bars are  
1002 medians and error bars are IQR.

1003

1004 **Figure 6. Endocytosis and Vesicle trafficking are essential for NB ingression.**

1005 **(A-C)** Loss of AP2 and Dyn function blocks endocytosis. (A) Whereas control NBs lose their apical  
1006 domain within ~24 min ( $n=40$  NBs, 2 embryos), knockdown of AP2 $\alpha$  (AP2 $\alpha$ -RNAi) results in significant  
1007 delays in ingression ( $n=87$  NBs, 4 embryos) or incomplete ingression, with 24% of NBs dividing on the  
1008 embryo surface (middle panels) and 14% of NBs apically constricted but failing to complete ingression  
1009 (lower panels). Membrane labeled with GAP43::mCherry, Scale bar, 5  $\mu\text{m}$ . (B) Quantification of  
1010 ingression dynamics of NBs in AP2 $\alpha$ -RNAi ( $n=66$  NBs, 3 embryos) versus control embryos ( $n=40$  NBs,  
1011 2 embryos). AP2 $\alpha$ -RNAi NBs show slower apical area loss and reduced amplitude of contractions

1012 compared to control. Control cells were only tracked until their apical domain reached  $9 \mu\text{m}^2$  (in contrast  
1013 to  $\sim 1.5 \mu\text{m}^2$  in other figures) as 38% of NBs in *AP2 $\alpha$ -RNAi* only constricted their apices to that value, but  
1014 not below. Median amplitudes of contractions for control or *AP2 $\alpha$ -RNAi*,  $4.1/3.0 \mu\text{m}^2/\text{min}$ , \*\*\*\*  $p=4 \times 10^{-6}$ ,  
1015 and expansions,  $1.5/1.5 \mu\text{m}^2/\text{min}$ , ns,  $p=0.88$  (KS test). Median durations of contractions for control or  
1016 *AP2 $\alpha$ -RNAi*,  $67.2/62.7$  sec; ns,  $p=0.22$ , and expansions,  $24/27.4$  sec, ns,  $p=0.27$  (KS test); 233–855  
1017 events per condition. (C) Mean apical area loss and total apical Crb levels during NB ingression in *Dyn<sup>TS</sup>*  
1018 (*shibire<sup>ts1</sup>* mutant) embryos at  $22^\circ\text{C}$  and  $32^\circ\text{C}$  (32 NBs from 3 embryos at  $22^\circ\text{C}$  and 31 NBs from 2  
1019 embryos at  $32^\circ\text{C}$ ). Lower panels show cross-sections of ventral ectoderm of stage 10 embryos expressing  
1020 the NB reporter HG4-1 at the permissive temperature ( $22^\circ\text{C}$ ) or restrictive temperature ( $32^\circ\text{C}$ ) where  
1021 some NBs failed to ingress (arrowheads).  $N=8$  and 11 *Dyn<sup>TS</sup>* embryos at  $22^\circ\text{C}$  and  $32^\circ\text{C}$ , respectively.  
1022 Apical side, up. Scale bar,  $15 \mu\text{m}$ .  $T=0$  min, onset of ingression; means  $\pm$  SEM.  
1023 (D) Rab5 activity promotes ingression. Mean apical area loss during NB ingression in embryos  
1024 expressing constitutive active Rab5-CA (58 NBs, 4 embryos) or normal Rab5 (Rab5-WT; control; 36  
1025 NBs, 3 embryos).  $T=0$  min, onset of ingression; means  $\pm$  SEM. Amplitude and duration of individual  
1026 apical contractions or expansions during ingression in Rab5-WT versus Rab5-CA embryos. Median  
1027 amplitude of contractions for Rab5-WT or Rab5-CA:  $2.4/3.3 \mu\text{m}^2/\text{min}$ ; \*\*\*\*,  $p=4.8 \times 10^{-5}$ . Median  
1028 duration of expansions for Rab5-WT or Rab5-CA:  $19/15$  sec ( $\log_{10}$ ), \*\*,  $p=1.4 \times 10^{-3}$  (KS test); 341-448  
1029 events per condition.  
1030 (E) Retromer limits ingression speed. Mean apical area loss during NB ingression and total apical Crb  
1031 levels in *Vps26<sup>mz</sup>* mutants (23 NBs, 5 embryos; mz indicates maternal-zygotic mutants) versus controls  
1032 (59 NBs, 12 embryos). Total intracellular levels of Crb in ingressed NBs from *Vps26<sup>mz</sup>* mutants (98 NBs,  
1033 7 embryos) and controls (115 NBs, 5 embryos).  
1034 (F) ESCRT enhances loss of apical Crb and apical membrane. Mean apical area loss during NB  
1035 ingression and total apical Crb levels in *Hrs<sup>mz</sup>* mutants (36 NBs, 7 embryos) versus controls (40 NBs, 5  
1036 embryos). Total intracellular levels of Crb in ingressed NBs from *Hrs<sup>mz</sup>* mutants (103 NBs, 6 embryos)  
1037 and controls (115 NBs, 5 embryos). In (E) and (F): Snail (blue) identifies NBs. Scale bar,  $5 \mu\text{m}$ .  $T=0$  min,  
1038 onset of ingression; means  $\pm$  SEM.

1039

1040 **Figure 7. Neur-dependent disruption of the Crb complex is essential for NB ingression.**

1041 (A) Loss of Sdt slows late ingression. Tukey's box-and-whisker plots of NBs ingression speed (apical  
1042 area reduction) in *sdt-RNAi* and controls embryos during early and late ingression. Medians ( $\mu\text{m}^2/\text{min}$ )  
1043 for control and *sdt-RNAi*:  $-1.3/-1.6 \mu\text{m}^2/\text{min}$  (early ingression), ns,  $p=0.44$  and  $-0.6/-1.3 \mu\text{m}^2/\text{min}$  (late  
1044 ingression), \*\*\*\*,  $p=1.9 \times 10^{-5}$  (KS test). *sdt-RNAi*: 54 NBs, 6 embryos; controls: 30 NBs, 4 embryos.



1045 **(B)** Quantification of total apical fluorescence levels for all Sdt isoforms (Sdt::GFP, 36 NBs, 6 embryos)  
1046 and for Sdt3 (Std3::GFP, 48 NBs, 6 embryos). T=0 min, onset of ingression; means +/- SEM.

1047 **(C)** Ingressing live NBs in Sdt3::GFP (control) and SdtΔ3::GFP embryos (dots, arrowheads). Sdt3::GFP  
1048 NBs lost their apical domain within ~33 min (top panels, 48 NBs, 4 embryos). Apical plugs formed in  
1049 SdtΔ3::GFP ingressing NBs (arrowheads in lower panels; 48 NBs, 4 embryos). Scale bar, 5 μm.

1050 **(D)** Mean apical area loss during NB ingression in Sdt3::GFP and SdtΔ3::GFP embryos. N values as in  
1051 (C). T=0 min, onset of ingression; means +/- SEM.

1052 **(E)** Quantification of apical area loss in 3 individual NBs from Sdt3::GFP (blue lines) and SdtΔ3::GFP  
1053 (red lines) embryos during ingression. SdtΔ3::GFP NBs maintain an apical plug for 30-40 minutes after  
1054 control cells have completed ingression. T=0 min, onset of ingression.

1055 **(F)** Quantification of total Sdt3::GFP and SdtΔ3::GFP fluorescence at the apical domain during  
1056 ingression. n values as in (C). T=0 min, onset of ingression.; means +/- SEM.

1057 **(G)** SdtΔ3::GFP embryos show reduced late ingression speed. Tukey's box-and-whisker plots of  
1058 ingression speed in Sdt3::GFP and SdtΔ3::GFP NBs during early and late ingression. Medians for  
1059 Sdt3::GFP and SdtΔ3::GFP: -1.4/-1.3 μm<sup>2</sup>/min (early ingression), ns, p= 0.12 and -0.8469/-0.4946  
1060 μm<sup>2</sup>/min (late ingression), \*\*, p= 1x10<sup>-3</sup>(KS test); n values as in (C).

1061 **(H)** Co-localization of SdtΔ3::GFP and Crb at apical plugs in stage 9 SdtΔ3::GFP embryos (arrowheads).  
1062 Scale bar, 5 μm.

1063 **(I)** Apical plugs in SdtΔ3::GFP embryos (arrowheads) do not contain Ecad. Dashed line indicates position  
1064 of ZX cross-section through an apical plug shown in the right panel (I') and schematic (I''). The apical  
1065 plug containing SdtΔ3::GFP (arrowhead) is positioned apically to Ecad/AJs (arrow). Dlg labels  
1066 basolateral membrane. Scale bars, 5 μm.

1067

1068 **Figure 8: Neur, but not Delta, is required for removal of Crb from the NB apical membrane during**  
1069 **ingression.**

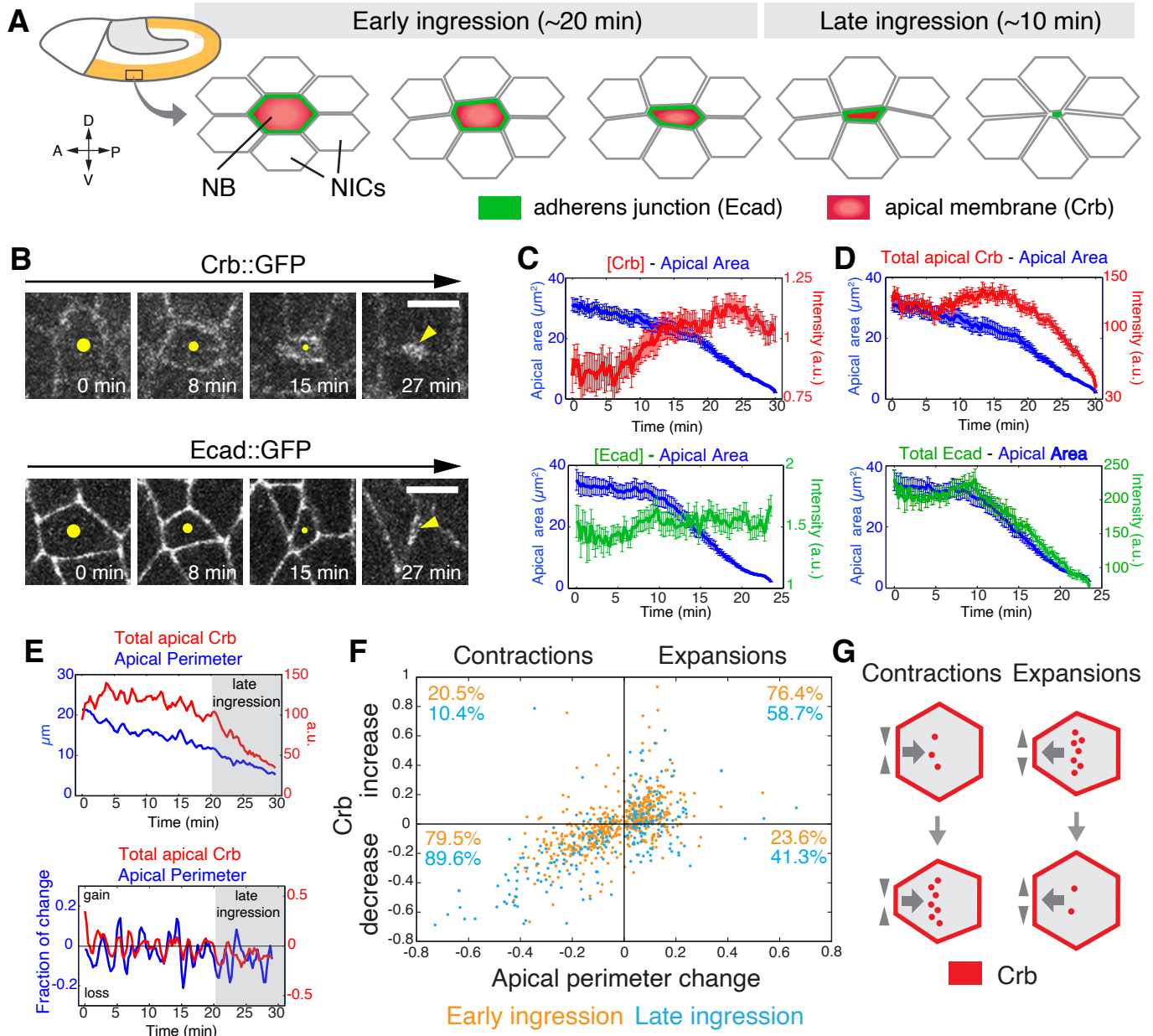
1070 **(A)** Endo-Crb::GFP embryos showing NBs clusters (circled) in *neur*-RNAi (20 NBs, 2 embryos) and  
1071 *Delta*-RNAi (20 NBs, 2 embryos) embryos. Note ectopic accumulation of apical Crb and slower  
1072 ingression with *neur*-RNAi compared to *Delta*-RNAi. Scale bar, 5 μm.

1073 **(B-C)** Total Crb::GFP (B) at apical domain (junctional and medial pools) and apical area loss (C) during  
1074 ingression in *neur*-RNAi (20 NBs, 2 embryos) and *Delta*-RNAi (20 NBs, 2 embryos) embryos. *Delta*-  
1075 RNAi was chosen as a control as it causes a neurogenic defect similar to *neur*-RNAi. Due to reduced

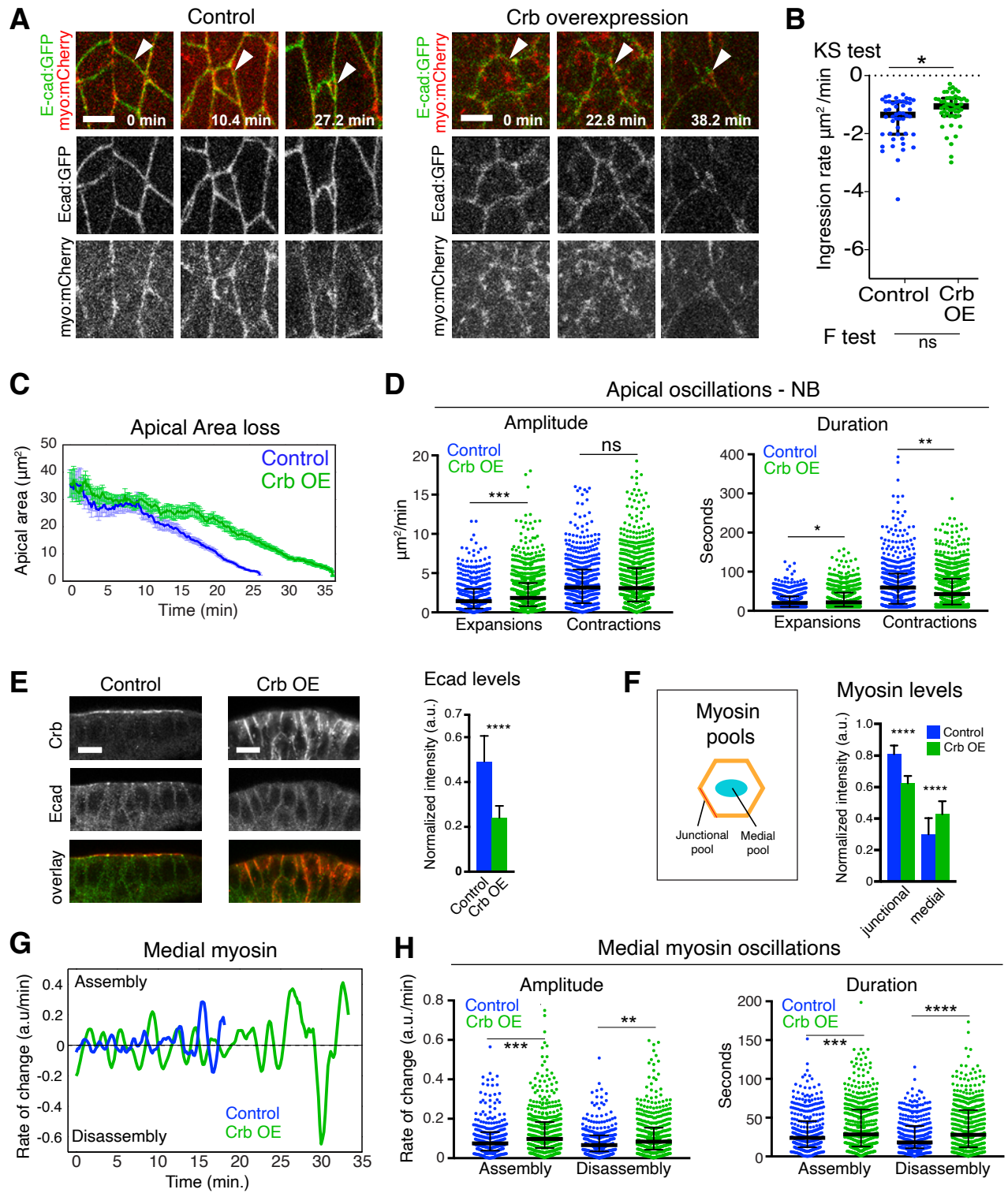
1076 levels of apical Crb in both conditions, the apical surface was traced starting at  $26 \mu\text{m}^2$  (mid-ingression,  
1077 T=0 min) in both data sets; means +/- SEM.

1078 **(D)** Amplitude and duration of apical contractions and expansions during NB ingression in *neur*-RNAi  
1079 versus *Delta*-RNAi embryos. Median amplitudes for *Delta*-RNAi and *neur*-RNAi for contractions,  
1080  $4.1/1.9 \mu\text{m}^2/\text{min}$ , \*\*\*\*  $p=9.6 \times 10^{-13}$ ; and expansions,  $2.3/1.3 \mu\text{m}^2/\text{min}$ , \*\*\*\*  $p=5.3 \times 10^{-6}$ , (KS test).  
1081 Median durations for *Delta*-RNAi and *neur*-RNAi for contractions, 39.3/38.4 sec; ns,  $p=0.88$ ; expansions,  
1082 16.6/24.1 sec, \*\*\*\*,  $p=8.2 \times 10^{-5}$  (KS test); n values as in (B); 230–440 events per condition. The median  
1083 amplitudes of apical contractions and expansions were reduced by 54% and 41%, respectively, in NBs of  
1084 *neur*-RNAi embryos, and the median duration of apical expansions was increased by 45% compared to  
1085 *Delta*-depleted controls.

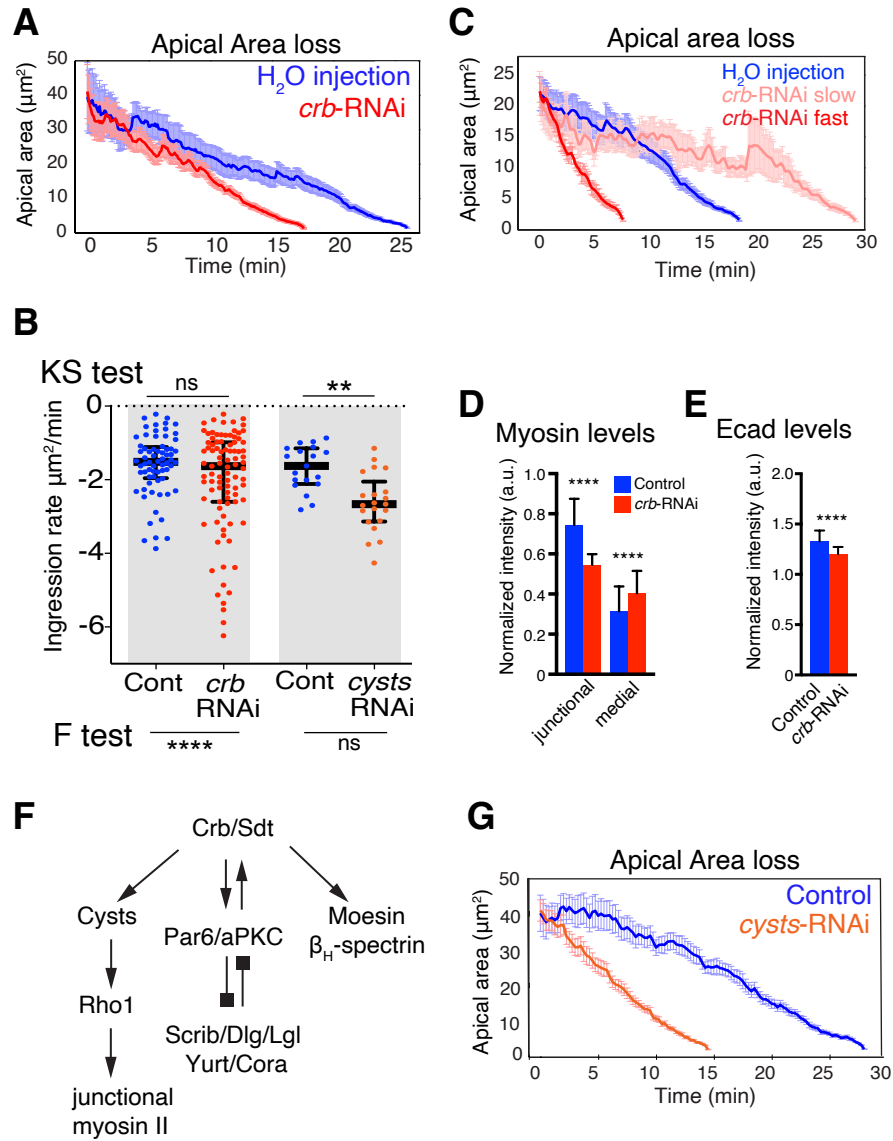
1086 **(E-F)** Crb endocytosis is reduced in *Sdt3* and *neur*-depleted embryos. Average total fluorescence of  
1087 intracellular Crb per NB after ingression (stage 9) in *Sdt3::GFP* (63 NBs, 3 embryos) and *Sdt3::GFP* (94  
1088 NBs, 4 embryos) embryos (E). Average total fluorescence of intracellular Crb per NB after ingression  
1089 (stage 9) in *neur*-RNAi (134 NBs, 7 embryos) and control (118 NBs, 6 embryos) embryos (F). Scale bar,  
1090  $5 \mu\text{m}$ . Means +/- SD. \*\*,  $p=3 \times 10^{-3}$ ; \*\*\*\*,  $p=4.5 \times 10^{-11}$  (2-tailed T test).  
1091  
1092



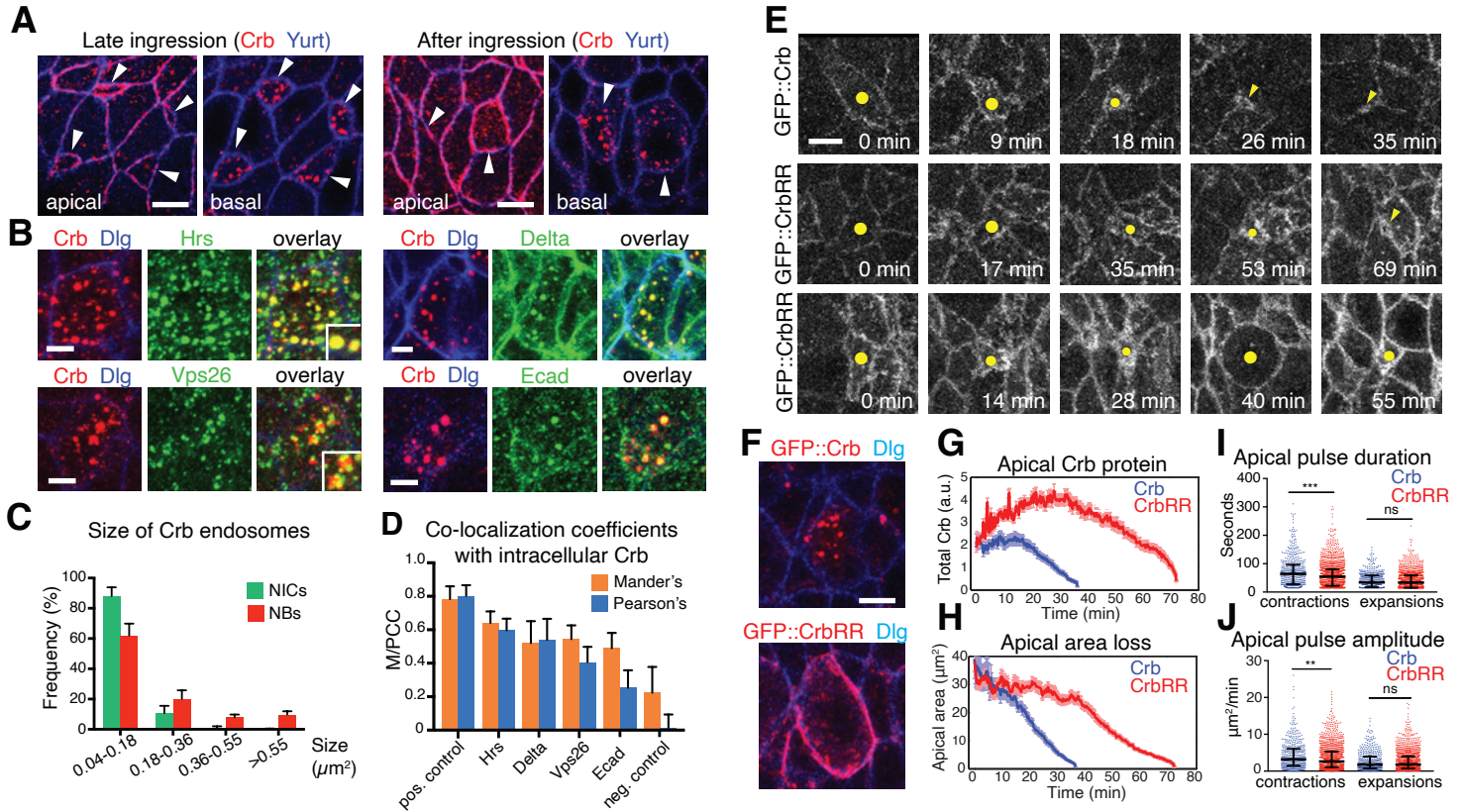
Simoes et al., Fig. 1



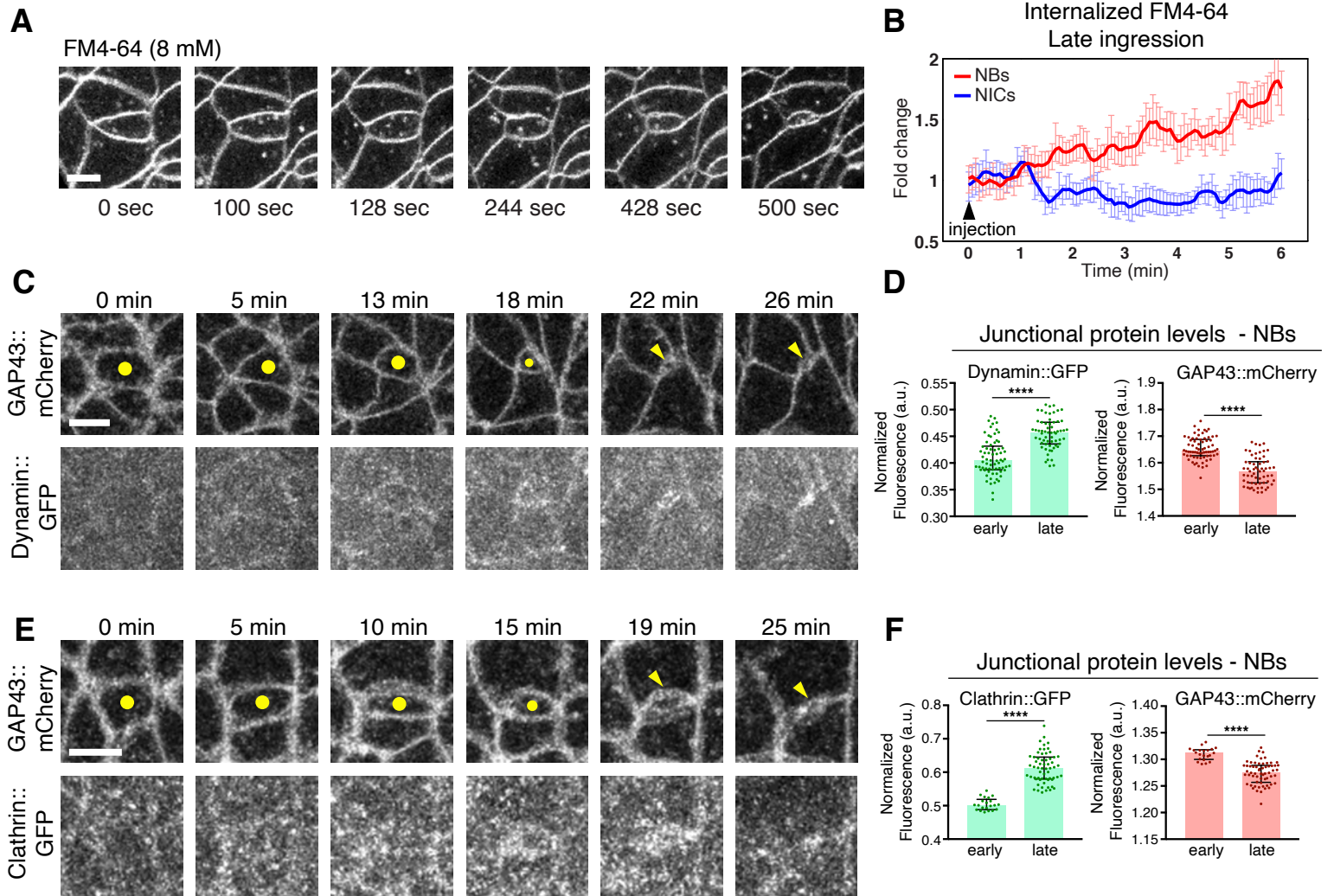
**Simoes et al. Fig. 2**



**Simoes et al., Fig. 3**

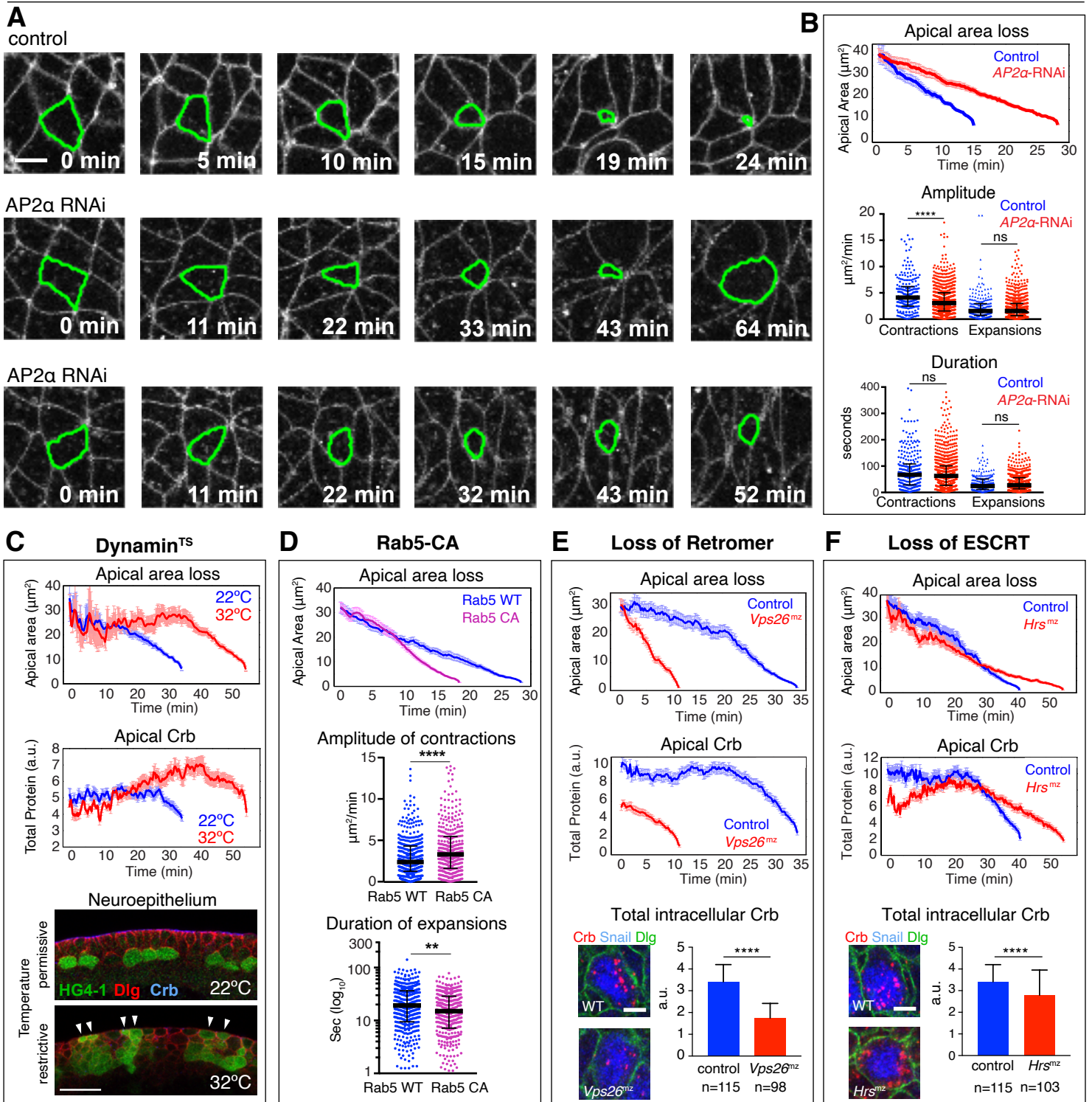


Simoes et al., Fig. 4



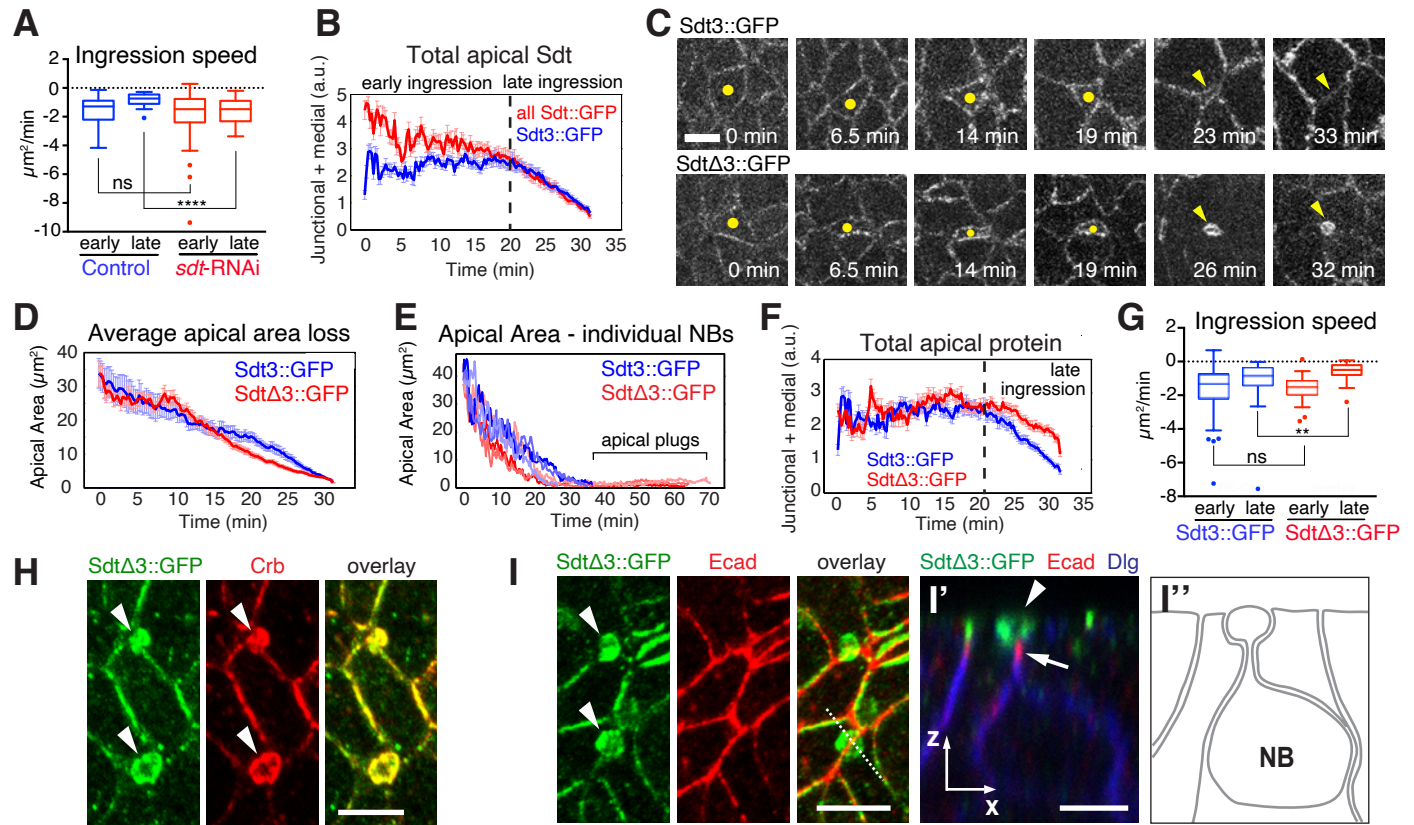
**Simoes et al. Fig. 5**

**AP2 $\alpha$ -RNAi**

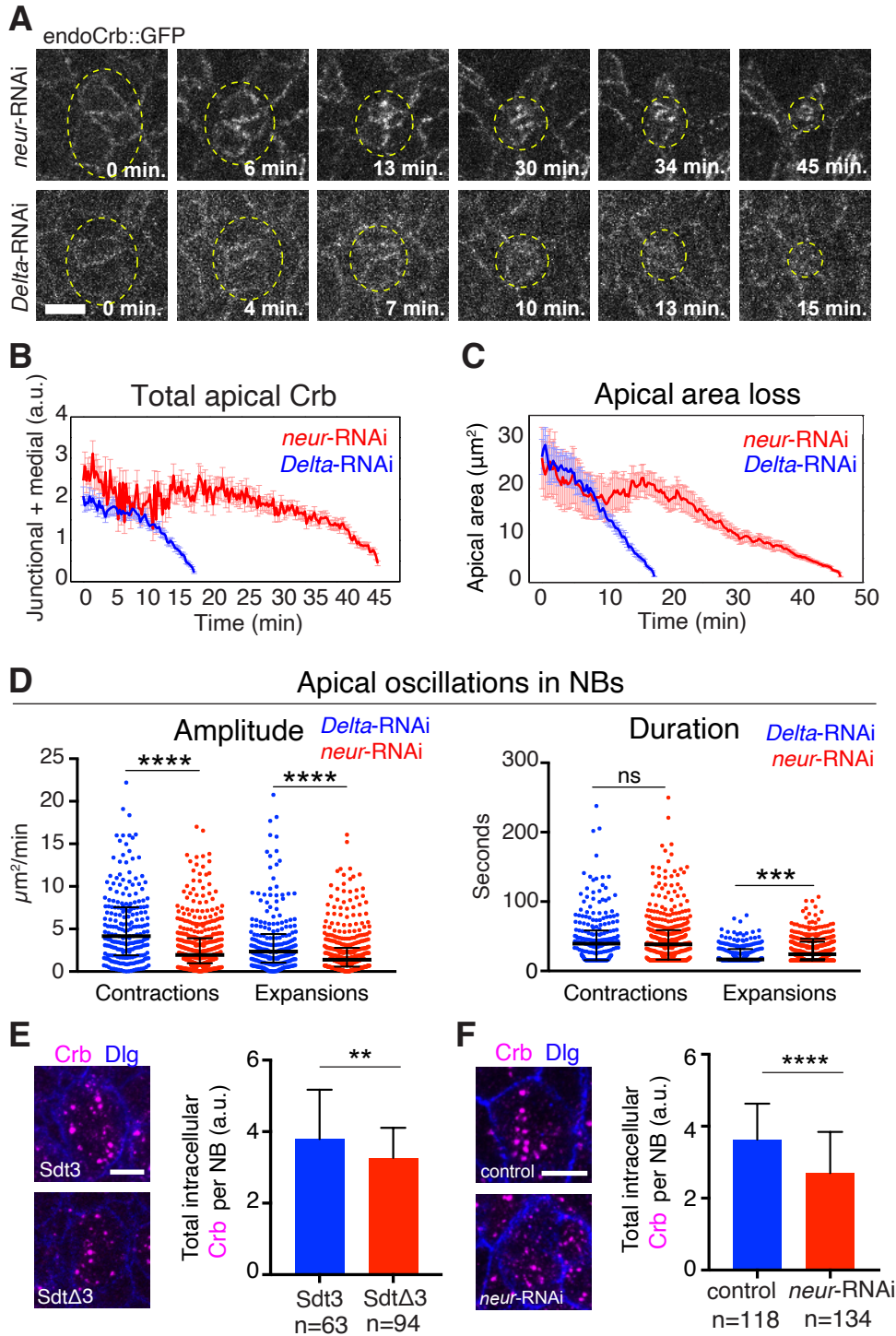


**Simoes et al., Fig. 6**





Simoes et al., Fig. 7



Simoes et al., Fig. 8